



# Gravity-driven film flow over isolated topography in a circular pipe

Joel P. Kuehner<sup>1</sup> and Isaiah R. Mefford<sup>1</sup>

<sup>1</sup>Department of Physics and Engineering, Washington and Lee University, Lexington, VA 24450, USA

Corresponding author: Joel P. Kuehner, [kuehnerj@wlu.edu](mailto:kuehnerj@wlu.edu)

(Received 30 August 2024; revised 17 December 2024; accepted 21 January 2025)

Gravity-driven film flow in circular pipes with isolated topography was examined with fluorescence imaging for three flow rates, two angles of inclination, and four topography shapes. The time-averaged free surface response in the vicinity of the topography depended on flow rate, inclination angle and topography shape. For some flow conditions, the time-averaged free surface included a capillary ridge, and for a subset of those conditions, a series of capillary waves developed upstream with a spacing often approximated by half the capillary length. In contrast to film flow over planar topography, the capillary ridge often formed downstream of the topography, and for the lowest flow rate over rectangular step down topography, the free surface developed a steady overhang along the downstream face of the topography. Possible dynamic causes of the unique film flow behaviour in circular pipes are discussed. Transient free surface fluctuations were observed at half the magnitude reported in film flow over corrugated circular pipes, and local maxima in transient magnitude corresponded to axial locations of inflection points in the time-averaged free surface. Local maxima are related to low surface pressure regions that vary in location and amplitude. Rectangular step down topography generated an extra ridge of fluid that formed on top of the capillary ridge for flow conditions, resulting in a capillary ridge downstream of the step. The extra ridge varied in temporal duration and spatial extent, and finds no comparison in planar film flow. No evidence of periodic behaviour was detected in the transient film response.

**Keywords:** thin films, capillary waves

## 1. Introduction

Film flows are found in a wide range of industrial, commercial, residential and natural settings. Industrial applications take advantage of the relatively large heat and mass

transfer coefficients associated with film flows, such as their effective use in heat pipes (Kwon, Kwon & Jung 2023) or over structured packings (Trifonov 2019; Iyer *et al.* 2021). Film flows are often employed in commercial and residential situations, for example, when cleaning and disinfecting (Landel & Wilson 2021) or cooking (Boujo & Sellier 2019). The natural environment includes numerous occurrences of film flows, whether in geological formation (Ledda *et al.* 2021) or avalanche development (Li *et al.* 2024), and biological systems rely upon their behaviour, for instance, prey fluid flowing along the deutosternal grooves on mites (Wernz & Krantz 1976; Flechtmann, Evans & McMurtry 1994; Bowman 2023), oxygen absorption within lung passageways (Si & Xi 2022), tear development atop the eye surface (Mehdaoui *et al.* 2021), or liquid transport across leaves (Glass *et al.* 2010). In many of these cases, the film flow is impacted by its interaction with the topography of the underlying substrate. This topography can incorporate isolated, non-uniform, or periodic structure that is either purposefully implemented or indirectly existent, and the effects on the film flow must often be addressed. Film flow over planar substrates, both with and without topography, has attracted significant attention in an attempt to understand both the steady and unsteady film flow behaviour (Craster & Matar 2009; Kalliadasis *et al.* 2012; Aksel & Schörner 2018). Despite the substantial amount of findings, investigations continue to expand the understanding of planar film flow, in particular its interaction with isolated disturbances (Singh & Tiwari 2024; D'Alessio 2024) and periodic topography (Al-Shamaa, Kahraman & Wierschem 2023).

In comparison, film flow in circular pipe geometries has received less attention, even though a notable number of applications exist in pipeline transport or similarly curved geometry. Investigations of film flow along circular geometry without topography have been conducted, such as the flow along the interior or exterior of a vertical circular pipe (Roy, Roberts & Simpson 2002; Lister *et al.* 2006; King *et al.* 2007; Camassa & Ogrosky 2015; Ma *et al.* 2020; Camassa *et al.* 2021, 2016), along a wire (Kalliadasis & Chang 1994; Kliakhandler, Davis & Bankoff 2001; Gabbard & Bostwick 2021), within a funnel (Lin, Dijksman & Kondic 2021; Xue & Stone 2021), or between vertical pipes (Wang *et al.* 2020). These investigations reveal that film flow behaviour within circular geometries differs in some ways from that found over planar substrates, such as the formation of collars and lobes along the film (Lister *et al.* 2006). The importance of topography along circular substrates is highlighted by its existence in applications such as bearing chambers (Eastwick, Bertin & Johnson 2006, 2005; Kneer *et al.* 2008; Li, Li & Wang 2022) or falling film evaporators (Åkesjö *et al.* 2023). Recently, gravity-driven film flow inside corrugated circular pipes was investigated to document and examine the characteristics of travelling waves specific to curved topographies (Kuehner, Mitchell & Lee 2019; Kuehner *et al.* 2021; Kuehner 2022). Beyond these corrugated circular pipe studies, the only other known film flow study over circular pipe substrates incorporating topography is for the exterior flow along a cylinder with a discontinuity in pipe radius (Khayat, Kim & Delosquer 2004). Additional work in circular geometries with topography will broaden the limited scope of available findings, further delineate the aspects of film flow in circular geometries that are not observed in planar cases, and potentially determine the phenomena that lead to these distinctions.

Film flow over planar substrates with isolated topography received early attention due to the importance of substrate defects on spin coating processes (Stillwagon & Larson 1990). Subsequent investigation of film flow over two-dimensional (2-D) planar step down topography indicated that the film develops a capillary ridge just prior to the step down for conditions in which surface tension is relevant and forms a depression in the free surface upstream of the capillary ridge as the angle of inclination of the substrate increases (Aksel 2000). The capillary ridge is of primary importance in studying film flow response to

isolated topography as it often represents the most prominent departure from upstream film thickness. The capillary ridge develops a favourable pressure gradient that drives the film around the corner of the step down topography (Mazouchi & Homsy 2001) and is associated with the formation of a separation eddy on the downstream face of the step (Gaskell *et al.* 2004b; Bontozoglou & Serifi 2008) or eddies within a rectangular trough (Scholle, Gaskell & Marner 2019). The elevation of the capillary ridge depends on the step height (Scholle *et al.* 2019; Kalliadasis, Bielarz & Homsy 2000; Mazouchi & Homsy 2001), angle of inclination (Pal, Sanyasiraju & Usha 2021) and surface tension (Mazouchi & Homsy 2001; Ovcharova 2006). For some flow conditions, a series of capillary waves can develop upstream of the capillary ridge as the film approaches a step down (Kalliadasis *et al.* 2000) or a rectangular trough (Pal *et al.* 2021). These capillary features, as well as similar depressions in film thickness and capillary waves downstream of a step down, have been observed in other numerical (Kalliadasis *et al.* 2000; Mazouchi & Homsy 2001; Bielarz & Kalliadasis 2003; Decré & Baret 2003; Gaskell *et al.* 2004b; Davis & Troian 2005; Bontozoglou & Serifi 2008; Veremieiev *et al.* 2010; Scholle *et al.* 2019; Pal *et al.* 2021, 2022) and experimental (Baret & Decré 2000; Decré & Baret 2003) investigations of 2-D planar step down or rectangular trough topographies, as well as over planar rectangular slits (Pettas *et al.* 2017). The downstream location of the capillary ridge varies with surface tension, inclination angle and flow rate (Aksel 2000; Bontozoglou & Serifi 2008), and the streamwise length of the capillary ridge scales with the capillary number (Mazouchi & Homsy 2001; Bontozoglou & Serifi 2008). Once formed, these free surface features are stable to disturbance (Kalliadasis & Homsy 2001; Bielarz & Kalliadasis 2003; Davis & Troian 2005); hence the steady-state free surface elevation profile retains importance even for unsteady flow conditions as the steady features remain after transient disturbances pass.

For film flow over a 2-D planar step up, the film develops a capillary ridge that precedes a decrease in film thickness before the film rises over the step (Fernandez Parent, Lammers & Decré 1998; Decré *et al.* 1999; Lucéa *et al.* 1999; Baret & Decré 2000; Mazouchi & Homsy 2001; Decré & Baret 2003; Gaskell *et al.* 2004b; Bontozoglou & Serifi 2008; Scholle *et al.* 2019; Pal *et al.* 2021, 2022), and these free surface features have similar dependencies on flow geometry and fluid properties as found for film flow over a step down. The curvature of the free surface develops to overcome the adverse pressure gradient that develops as the film is forced up over the step, and is again related to the existence of separation eddies near the corners of the topography (Bontozoglou & Serifi 2008). For film flow over a 2-D obstacle, the film thickness tends to decrease before forming a capillary ridge just prior to the obstacle (Bonart & Repke 2018; Kalliadasis *et al.* 2000; Pal *et al.* 2022), in contrast to the flow over a step up. However, similar to the step up, flow over an obstacle is also affected by the formation of eddies upstream and downstream of the obstacle (Higdon 1985; Hansen 1991). As found for the step down and rectangular trough topographies, the importance of surface tension is again noted for film flow over obstacles. While surface tension must exist to form the capillary features along the free surface, as surface tension continues to increase, it acts to eventually flatten and smooth the free surface over the obstacle (Hansen 1986, 1991; Kalliadasis *et al.* 2000).

For film flows in many natural settings, such as for shallow rivers or for glacial movement, it is uncommon to know the substrate topography *a priori*; hence it is advantageous to be able to deduce the topography along a river bed or atop the bedrock supporting a glacier from the flow response to the topography. Analytical and numerical approaches have been applied to determine the substrate topography from the free surface shape (Sellier 2008; Sellier & Panda 2010) or from the free surface flow velocity (Heining, Pollak & Sellier 2013; Heining & Sellier 2017), both of which are more readily measured in the field. These analytical and numerical methods can then be employed

by those designing substrates for industrial applications to produce a desired coating response (Sellier 2008; Sellier & Panda 2010). In addition, as substrate topography can modify the manner in which instabilities form, such as rivulets (Slade *et al.* 2013), these inverse methods afford the designer another means of enhancing heat or mass transfer by purposely inducing instabilities. The development of inverse methods is informed and validated by investigations into film flow behaviour over known topography, highlighting the importance of continued investigation of film flows in circular pipe geometries for which inverse methods have yet to be developed.

The response of film flow to isolated substrate topography was expanded to include three-dimensional (3-D) geometry such as trenches and obstacles that have a finite width. For numerical simulations of film flow over 3-D obstacles, the film develops a capillary ridge over the obstacle, with a depression just prior to the obstacle (Hayes, O'Brien & Lammers 2000; Bielarz & Kalliadasis 2003; Gaskell *et al.* 2004b; Blyth & Pozrikidis 2006; Baxter *et al.* 2009; Veremieiev *et al.* 2011, 2015) similar to film flow response to 2-D obstacles. The capillary ridge extends around the sides of the 3-D obstacle, forming a horseshoe shape, and the results afford a perspective of the horseshoe wake that forms around a depression in film thickness axially downstream of the obstacle (Blyth & Pozrikidis 2006; Baxter *et al.* 2009; Gaskell *et al.* 2004b, 2012). The existence of these features depends upon the thickness of the film in comparison to the height of the obstacle and whether inertia is considered in the analysis (Pozrikidis & Thoroddsen 1991; Peurrung & Graves 1993). Additionally, the features are modified if the film is volatile and dries while forming (Peurrung & Graves 1991). Similar to the film response to 2-D planar topography, as surface tension increases, the elevation of the capillary ridge upstream of the 3-D obstacle decreases (Pozrikidis & Thoroddsen 1991; Blyth & Pozrikidis 2006), and the balance between angle of inclination and the magnitude of surface tension determines whether the capillary ridge forms at all (Gaskell *et al.* 2004b; Scholle *et al.* 2019).

Film flow over a 3-D rectangular trough produces a free surface with a capillary ridge just prior to the trough that wraps around the side of the trough in a horseshoe shape referred to as a bow wave (Lucéa *et al.* 1999; Decré & Baret 2003; Bielarz & Kalliadasis 2003; Gaskell *et al.* 2004b, 2012; Lee, Thompson & Gaskell 2007; Veremieiev *et al.* 2010; Cowling *et al.* 2011; Veremieiev, Thompson & Gaskell 2015; Pal *et al.* 2021, 2022; D'Alessio 2024). The film rises into a second ridge at the outlet of the trough because fluid enters the trough over the upstream and side edges, while only exiting the trough along the downstream edge (Gaskell *et al.* 2004b). The difference between inlet and outlet flow areas can lead to the outlet ridge being as or more prominent than the capillary ridge that precedes the topography (Decré & Baret 2003; Gaskell *et al.* 2004b; Lee *et al.* 2007; Cowling *et al.* 2011; Pal *et al.* 2021, 2022). If the rectangular trough is wide enough in the spanwise direction, the outlet ridge can split into two separate ridges (Gaskell *et al.* 2004b; Veremieiev *et al.* 2010; Pal *et al.* 2021, 2022), further indicating the relevance of inlet to outlet area for flow through the trough. Film flows over troughs with different 3-D cross-sectional shapes, such as circular or diamond troughs, produce film flow responses similar to those of the rectangular trough (Lucéa *et al.* 1999; Lee *et al.* 2007). In agreement with the findings for 2-D planar cases, the free surface features caused by isolated 3-D troughs are stable to inlet disturbances (Lee *et al.* 2007) and are dependent upon the vortex structure that forms in the trough (Gaskell *et al.* 2012; Veremieiev, Thompson & Gaskell 2012). Owing to the horseshoe capillary ridge and wake structure, the film flow over isolated 3-D troughs produces capillary effects that are sustained further downstream than is found for the corresponding 2-D planar geometries (Decré & Baret 2003; Gaskell *et al.* 2004b).

Beyond film flow over topography, planar film flow around occlusions has also been examined. As occlusions can be used to divert natural film flows, such as for lava or avalanches, understanding the response of a film flow to occlusions can reveal important design considerations (Hinton, Hogg & Huppert 2019). Investigations of films interacting with 3-D occlusions have included isolated circular, elliptical or square cylinders as well as collections of cylinders (Kneer *et al.* 2008; Lee, Thompson & Gaskell 2008; Gaskell, Lee & Thompson 2010; Veremieiev *et al.* 2011; Hinton *et al.* 2020*b*). Film flow around corners is also examined in the same manner (Hinton *et al.* 2020*a*; Jensen, Chini & King 2004). The isolated topography applied within the circular pipe geometry of the current work presents a substrate that incorporates both 2-D and 3-D planar film flow considerations, as the film along the pipe centreline must navigate over the centreline crests in the topography, and the film along the circumferential edge of the film must flow around the radial edge of each crest. Hence the observations for film flow over 2-D and 3-D planar obstacles and troughs are as relevant to the current findings as investigations of planar film flow around 3-D occlusions.

Another relevant class of film flows is that of a film spreading over a substrate with or without topography. These types of spreading films are typically examined in the context of coating technologies, such as spin coating; however, the unsteady behaviour of a moving contact line remains indirectly related to the transient response of film flows in circular pipes with isolated topography. In particular, if the circumferential extent of the free surface varies in time, then the edges of the film continually progress and recede along the substrate topography, approximating an oscillating contact line. Unsteady, periodic movement of the film flow in corrugated circular pipes has been documented (Kuehner *et al.* 2019, 2021; Kuehner 2022); hence similar spreading motions might exist in the present film flow. Transient spreading of films or droplets is a typical contact line problem that is examined with (Glass *et al.* 2010) or without (Bertozzi & Brenner 1997; Gramlich, Mazouchi & Homsy 2004; Gaskell *et al.* 2004*a*; Mazouchi, Gramlich & Homsy 2004; Lee, Thompson & Gaskell 2011; Mazloomi & Moosavi 2012, 2013; Lampropoulos, Dimakopoulos & Tsamopoulos 2016; Karapetsas *et al.* 2017; Singh & Tiwari 2024) the effects of evaporation. Of relevance to the current work is the capillary ridge that forms at the leading edge of these spreading films, and its interaction with topography (Gramlich *et al.* 2004; Mazouchi *et al.* 2004; Mazloomi & Moosavi 2012, 2013; Lampropoulos *et al.* 2016; Karapetsas *et al.* 2017).

One of the key findings in gravity-driven film flow in corrugated circular pipes was the formation of periodic travelling waves that arise from ambient sources (Kuehner *et al.* 2019, 2021; Kuehner 2022). In comparison to that found for film flow over 2-D planar corrugations (Vlachogiannis & Bontozoglou 2002; Argyriadi, Vlachogiannis & Bontozoglou 2006; Plumerault, Astruc & Thual 2010; Cao, Vlachogiannis & Bontozoglou 2013), an increased robustness of the process that generates travelling waves from ambient sources was demonstrated through a lack of frequency dependence on flow rate or inclination angle (Kuehner *et al.* 2019). The corrugated circular pipe findings provide a motivating factor for pursuing the current work, namely to understand whether there are flow features that develop from isolated topography in circular pipes that could be involved in the resonance that leads to periodic travelling waves when the isolated topography is periodically repeated as corrugations. Previous planar investigations have highlighted how planar film flow responds to a patterned surface, such as a circuit structure, for which the free surface develops as a combination of flow features identified for the film encountering isolated circuit elements (Lee *et al.* 2008). Similarly, the manner in which a film proceeds over two obstacles on a planar substrate incorporates the features of the film response to isolated obstacles while including capillary features that do not exist for the isolated

obstacles (Pritchard, Scott & Tavener 1992). Film flow response to groupings of 3-D troughs further demonstrates how the surface features generated by isolated topography can be incorporated into the film response to patterned topography, yet features not seen in the isolated cases also appear (Lee *et al.* 2007). Hence results for planar topography further motivate the current work and indicate that the findings for isolated topography in circular pipes might expand on the understanding of the film flow response to corrugated circular pipes.

Therefore, we aim to examine whether step down and single trough substrate geometries in circular pipes generate a film flow response that is unique in comparison to the planar cases, and to investigate whether the film response to isolated topography could potentially contribute to the distinctive periodic behaviour seen in corrugated circular pipes. In the present paper, we describe the geometry and fabrication of the circular pipes with isolated topography, as well as the fluorescence imaging and analysis methods in § 2. The results of the film flow measurements, including the time-averaged and transient features of the free surface, are analysed and discussed in comparison to film flow over planar substrates and corrugated circular pipes in § 3, and the conclusions from the findings are summarized in § 4.

## 2. Experimental facilities and methods

A schematic representation of the experimental set-up is presented in [figure 1](#) for the case of the film flow in a circular pipe encountering a rectangular step down, which occurs as a discontinuity in pipe radius. The water delivery system is similar to that used in our previous work (Kuehner *et al.* 2019, 2021; Kuehner 2022) in which water is pumped from a large lower reservoir (not shown in [figure 1](#)) into an overflow reservoir. As the water exits the overflow reservoir, it is guided into the circular pipe by a short, curved plastic sheet. The volume flow rate  $Q$ , ranging between 0.116 lpm and 0.210 lpm, is measured just prior to the overflow reservoir using a variable-area flow meter with uncertainty 0.01 lpm. We utilize a selection of volume flow rates similar to those in our previous work to better permit comparison to those results. Due to the curvature of the pipe, the thin film of water flows axially downwards along a narrow central portion of the pipe before reaching the isolated topography. Hence the incoming spanwise width of the free surface, approximately 13–16 mm, is far less than typically studied in 2-D or 3-D planar cases (Leontidis *et al.* 2010). The schematic includes a representation of the film surface rising through a capillary ridge near the topography. For the cases of the step down topographies, the water spreads in the circumferential direction at the bottom of the topography before again forming a narrow film that flows axially towards the exit of the pipe. For the trough topographies, the water fills the trough, widening the film surface in the spanwise direction beyond the circumferential spreading for the step down topographies, before again forming a narrow stream. The water that leaves the pipe is guided into the lower reservoir using flexible sheeting (not shown in [figure 1](#)) to reduce the effects of the impact on the free surface of the lower reservoir. The water in the closed-loop system is permitted to reach thermal equilibrium with the lab environment for at least 24 hours prior to data collection, and the flow system is operated for at least 20 minutes prior to data collection to ensure that the supply system has reached steady-state conditions. Similar to our prior experiment (Kuehner 2022), we focus on two angles of inclination for the circular pipe,  $\alpha = 15.3^\circ$  and  $20.3^\circ$  measured with a digital level with uncertainty  $0.2^\circ$ .

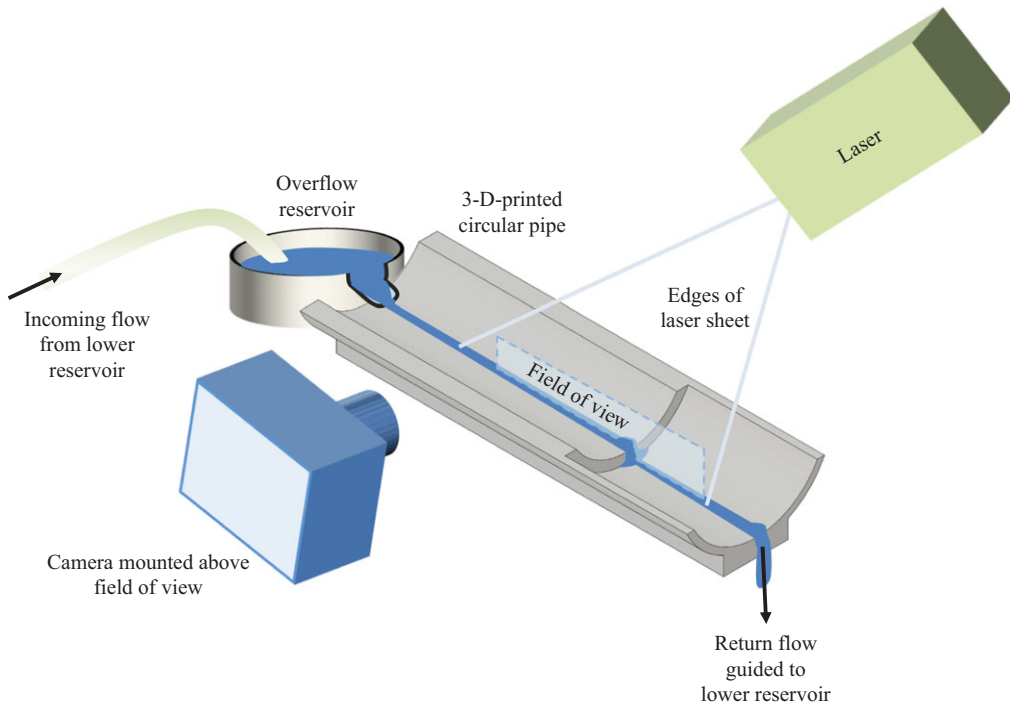


Figure 1. Schematic of the experimental flow apparatus with an approximation of water location within the circular pipe for a rectangular step down topography. Laser and laser sheet edges are indicated, and the portion of the laser sheet that is captured by the field of view of the camera is shown. The camera is mounted above the pipe and inclined downwards towards the field of view at an angle that is accounted for in calibration.

### 2.1. Pipe geometry and fabrication

Circular pipes with four different isolated topography shapes were utilized as the substrates for the current study. The axial geometry of each substrate is shown in [figure 2](#) and will be referenced with the following abbreviations: rectangular step down (RSD), triangular step down (TSD), rectangular trough (RTR), and triangular trough (TTR). As the original experiments focused on periodic corrugations, the isolated topography examined in this study was developed using the shape and terminology of the periodic corrugations utilized previously ([Kuehner 2022](#)). The quantities for the dimensions shown in [figure 2](#) are  $a = 1.9$  mm and  $L = 7.6$  mm, which are the same as those employed in the corrugation shape and tip width investigation ([Kuehner 2022](#)). The depth of each substrate topography is equivalent to  $2a$ . The length of the rectangular trough is  $3L/4$  and of the triangular trough is  $L$ , in accordance with the definition of a substrate wavelength in previous work ([Kuehner 2022](#)). Each pipe has average diameter  $D = 50.8$  mm, and the water travels approximately 90 mm before reaching the isolated topography, followed by approximately 40 mm before the end of the pipe. Based on preliminary findings and the results presented below, these distances ensure that the film interaction with the entrance or exit of the pipe does not interfere with the film response to the isolated topography.

To permit comparison with previous work and to develop a uniform method for categorizing the results between topographies, a length scale is needed to define the Reynolds number. In planar experiments, the Reynolds number is typically defined by utilizing the flow rate per width of the planar channel. For circular pipes with topography,

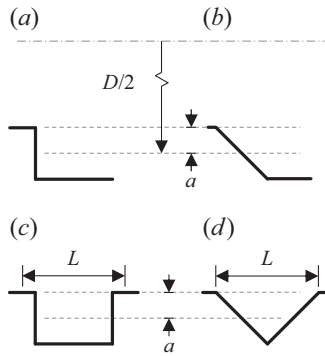


Figure 2. Axial variations of topography shape for (a) rectangular step down (RSD), (b) triangular step down (TSD), (c) rectangular trough (RTR), and (d) triangular trough (TTR) topographies. Substrate amplitude  $a$  and axial length  $L$  are shown. Average pipe diameter  $D$  and the pipe centreline are included only in the top row of substrates, and are similarly defined for all substrates.

the flow develops a variable width as it progresses through geometries of differing radial extent. In previous work in corrugated circular pipes, we defined a reference span  $b$  as the width of the water that fills a trough up to the crest without a consideration for the formation of a meniscus (Kuehner *et al.* 2019). Figure 3 displays the relevant pipe geometry for defining this reference span similar to that presented in previous work (Kuehner *et al.* 2019). The right triangle defined in figure 3(b) provides the dimensions that inform the relation for the reference span, resulting in  $b = \sqrt{8Da}$ . Hence  $b = 27.8$  mm for the given pipe dimensions. This reference span is directly applicable to the RTR and TTR topographies; however, while the water spreads in the circumferential direction at the bottom of the RSD and TSD topographies, it does not develop a width similar to the reference span. Motivated to ensure uniformity of the upstream conditions for the step down and trough topographies, and to align with the definitions utilized in our previous reports, we use the definition for the reference span for all topographies even though this span is not directly applicable to the step down topographies. Therefore, the Reynolds number will be defined as  $Re = q/\nu = Q/b\nu$ , with relevant fluid properties provided in table 1. Uncertainty in Reynolds number is propagated from the uncertainty in flow rate provided above, and that for the pipe geometry as defined in the next subsection.

The circular pipes are developed by revolving the axial substrate profiles shown in figure 2 around the central axis, then 3-D-printing the shape with the upper portion of the pipe removed for imaging purposes, as presented in figure 1. The pipes are printed from opaque dark grey ASA (acrylonitrile styrene acrylate) using the same 3-D printer settings utilized in all previous experimental work (Kuehner *et al.* 2019, 2021; Kuehner 2022) to ensure that substrate surface material and texture remain similar. The 3-D printer has spatial accuracy 0.2 mm, and slice height 0.127 mm was employed for each pipe, resulting in a maximum uncertainty in substrate dimensions of 0.2 mm.

## 2.2. Free surface and film thickness fluorescence imaging

The free surface of the film flow and the location of the substrate are identified using fluorescence imaging. Similar to previous experiments (Kuehner *et al.* 2019, 2021; Kuehner 2022), Rhodamine 640 perchlorate dye is mixed with the water, and fluorescence from the dye is excited using a continuous-wave laser (Coherent Genesis) with power levels ranging between 600 and 700 mW. The output of the laser is formed into a thin sheet by a combination of spherical and cylindrical lenses, and aligned with the axial centreline

Property	Symbol	Definition	Value/range	Units
Density	$\rho$		1000	$\text{kg m}^{-3}$
Kinematic viscosity	$\nu$		$1 \times 10^{-6}$	$\text{m}^2 \text{s}^{-1}$
Surface tension	$\sigma$		0.0727	$\text{N m}^{-1}$
Thin film parameter	$\delta$	$2\pi h_N/L$	0.36–0.43	
Volume flow rate per unit span	$q$	$Q/b$	69–125	$\text{mm}^2 \text{s}^{-1}$
Nusselt thickness	$h_N$	$(3\nu q/g \sin \alpha)^{1/3}$	0.43–0.53	mm
Average Nusselt velocity	$u_N$	$q/h_N$	161–239	$\text{mm s}^{-1}$
Axial capillary length	$L_{ca,a}$	$(\sigma/\rho g \sin \alpha)^{1/2}$	4.6–5.3	mm
Normal capillary length	$L_{ca,n}$	$(\sigma/\rho g \cos \alpha)^{1/2}$	2.8	mm
Viscous length	$L_\nu$	$(\nu^2/g)^{1/3}$	0.05	mm
Reynolds number	$Re$	$q/\nu$	69–125	
Froude number	$Fr$	$u_N^2/h_N g \cos \alpha$	7–11	
Kapitza number	$Ka$	$\sigma/\rho g_x^{1/3} \nu^{4/3}$	4833–5295	
Weber number	$We$	$\sigma/\rho u_N^2 h_N$	2.4–6.5	

Table 1. Characteristic properties and non-dimensional parameters.

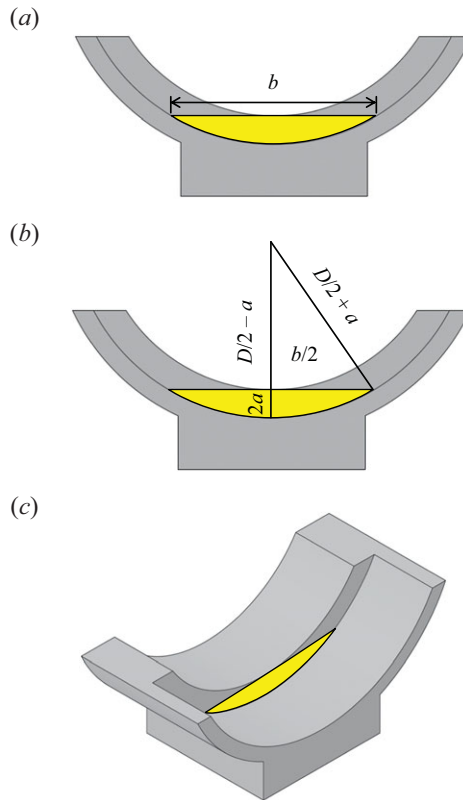


Figure 3. Schematic displaying (a) an upstream facing view of the yellow circular segment that identifies the reference span  $b$ , (b) the pipe geometry used to define the reference span as the chord associated with the yellow circular segment, and (c) an isometric view of the yellow circular segment within the topography.

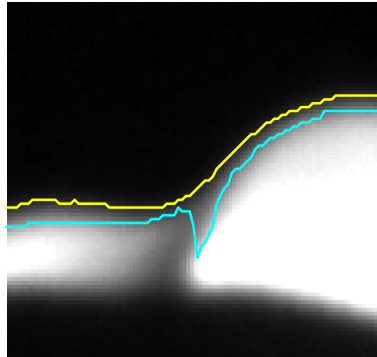


Figure 4. Comparison of the edge-detection results using the Canny method (cyan line) and the results using the c.d.f. method (yellow line) for an instantaneous image just upstream of the RSD topography for  $Re = 69$  and  $\alpha = 15.3^\circ$ .

of the circular pipe, as displayed in [figure 1](#). Images of the fluorescence were captured using a high-speed camera, also shown in [figure 1](#), and calibrated with an alignment target to correct for the off-axis image plane. The spatial resolution of the fluorescence images is estimated from the calibration as 0.031 mm per pixel. Time sequences of 23 808 images are acquired at 50 frames per second, representing almost 8 min of film flow behaviour. A red filter is applied to the camera lens to reduce the 488 nm laser excitation wavelength within the images.

The observed free surface of the film flow included undulations of a shorter wavelength as compared to previous work, in particular for the RSD topography. Even after adjusting the angle between the radial direction and the approach of the laser sheet to minimize the formation of low-intensity regions within the fluorescence images, the curvature of the free surface caused notable fluctuations in intensity. The intensity variations prompted adjustments to the free surface detection algorithms utilized previously, which were based on the Canny method (Kuehner *et al.* 2019, 2021; Kuehner 2022). While the Canny method is generally reliable even where large intensity gradients exist, it produced film surfaces that included defects which were difficult to distinguish from true surface undulations as could be accomplished previously. An example of a defect is presented in [figure 4](#) for a film flow just upstream of the RSD topography. The Canny-based method, shown in cyan in [figure 4](#), incorrectly identifies the free surface in the middle of the image that could not be corrected with our prior approach. Hence a new edge detection method was developed, shown by the yellow line in [figure 4](#), that relies upon the cumulative distribution function (c.d.f.) of the image intensity within a column of pixels in the radial direction. A spatial derivative was applied to the c.d.f. in the radial direction to locate the region where the c.d.f. first plateaus. Additionally, the results of the spatial derivative of the c.d.f. were useful in identifying and discarding errant free surface results in regions of low intensity. If the spatial derivative of the c.d.f. for a particular column did not indicate a clear plateau in the c.d.f., then the edge-detection results for that column were discarded, and the edge-detection results in the near vicinity were utilized to approximate the free surface in the discarded region. We found this method to be more sensitive and reliable for most of the images obtained in the current work; however, we note that the method is sensitive to edges only in the radial direction. While limited in scope, the ability to detect and correct surface defects outweighed the lack of sensitivity to free surface edges in the axial direction, given the nature of most of the images acquired in the current work. Three data sets included images for which this new c.d.f.-based method had to be further modified, as discussed

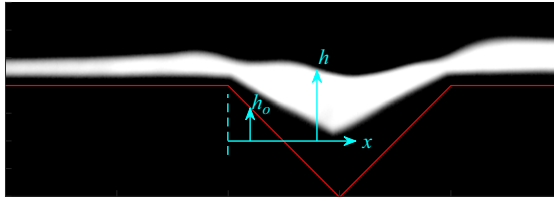


Figure 5. Instantaneous fluorescence image of film flow over TTR topography. The red line indicates the approximated location of the substrate. The coordinate system employed for axial distance  $x$ , absolute free surface elevation  $h$ , and substrate elevation  $h_0$  is shown. The fluorescence within the volume of the film is viewed through the non-uniform free surface, causing a distortion that makes the bottom of the water appear detached from the substrate.

Quantity	Uncertainty
Pipe geometry	$\pm 0.2$ mm
Lengths from images	$\pm 0.04$ mm
Film thickness	$\pm 0.15$ mm
Flow rate	$\pm 0.01$ lpm
Reynolds number	$\pm 6$
Inclination angle	$\pm 0.2^\circ$

Table 2. Summary of measurement uncertainty.

further in § 3. The results of the new c.d.f.-based method shown in figure 4 demonstrate the ability to avoid the surface defect as well as to better capture the free surface at the left-hand edge of the image. Comparing the results of the two methods across a range of flow conditions reveals that for instantaneous images, the c.d.f.-based method differs from the Canny-based method by approximately 4 pixels in regions of the free surface including substantial curvature, and typically by 1 pixel when the free surface curvature is similar to that seen in our previous work.

Once image acquisition was completed for a particular flow rate, angle of inclination, and topography shape, the pump was turned off and the remaining water within the pipe was allowed to drain until the film thickness on the pipe surface had reached a steady minimum within the limits of surface tension. Employing a method developed in our previous work (Kuehner 2022), we acquired fluorescence images of the remaining water in the pipe, and used these images to approximate the location of the first crest of the topography. By incorporating the known geometry of the 3-D-printed circular pipes, an approximation for film thickness can then be acquired. The axial origin for the coordinate system employed in the figures presented in § 3 is located at the start of the topography, as shown in figure 5. The elevation coordinate origin is at the average radius of the pipe, allowing the film thickness to be calculated as  $h - h_0$ . Based on the spatial resolution of the calibrated fluorescence images, we estimate the uncertainty for a length determined from an image to be 0.04 mm, and owing to the approximate nature of identifying the substrate, the uncertainty in film thickness is estimated to be 0.15 mm.

### 2.3. Measurement uncertainty

The measurement uncertainties presented in this subsection, along with those propagated for quantities discussed in this subsection and in § 3, are presented in table 2. Propagation methods for each uncertainty calculation are described where relevant.

### 3. Results and discussion

The free surface response of gravity-driven film flow through circular pipes with isolated topography was investigated for three volume flow rates, two inclination angles, and four variations in substrate topography. For consistency, the colours and markers utilized in the figures below are the same as those used in our previous report on corrugation shape and tip width (Kuehner 2022). As discussed in § 1, investigations into planar film flow over isolated topography have indicated that the film flows are stable (Kalliadasis & Homsy 2001; Bielarz & Kalliadasis 2003; Davis & Troian 2005), so the steady-state free surface profile will be regained after a disturbance passes. Hence we begin by presenting the steady-state response of the film flow to the topography before exploring the characteristics of the transient response that might relate to the periodic flow observed in corrugated circular pipes.

#### 3.1. Time-averaged free surface response

To develop a measure of the steady-state free surface response to the substrate topography, time-averaged absolute free surface elevations are calculated and presented in figure 6 for the full axial length under consideration. In the region upstream and downstream of the topography, the elevation and shape of the free surface are similar between flow rates and angles of inclination for a given topography, and display only minor variations between topographies, indicating that the response to the topography is primarily localized to the axial region surrounding the topography itself. For the RSD, TSD and TTR topographies, the film rises through a crest between  $x/L = 3.0$  and  $x/L = 4.5$  before travelling towards the exit of the pipe. This downstream crest is not observed in 2-D planar flows with similar topography, yet it is reminiscent of the ridge that forms at the outlet of a 3-D planar trough although of reduced magnitude (Gaskell *et al.* 2004b). The similarity to the 3-D case indicates that this downstream rise possibly results from the water leaving the step or trough region and having to decrease in spanwise extent to reach a narrow spanwise width similar to that upstream of the topography. This confluence of the downstream flow entering the topography with the spanwise flow from the regions where the water has spread circumferentially would compare to the effect observed for 3-D planar rectangular troughs, for which the flow enters over three sides of the rectangular trough but exits over one side (Gaskell *et al.* 2004b). The lack of this downstream rise for the RTR topography indicates that the flow in the spanwise direction might differ from that associated with the other topographies.

In the vicinity of the topography, the axial region identified by  $x/L = -0.5$  to  $x/L = 1.5$ , the free surface of the film varies notably with flow rate, angle of inclination and topography shape. These same variations in flow conditions also influenced the time-averaged free surface response for film flow within corrugated circular pipes (Kuehner 2022), indicating potentially similar effects in the underlying film flow. To better examine the time-averaged free surface response to the topography, figure 7 displays the time-averaged absolute free surface elevation profiles within this region. There is significant variation in free surface shape between flow conditions for the RSD topography (figure 7a). For the lowest and highest flow rates, and larger inclination angle, the free surface develops a series of capillary waves before rising into the capillary ridge over the RSD topography. The curvature of the capillary ridge develops a region of high free surface pressure that turns the flow around the steep RSD topography (Mazouchi & Homsy 2001). The circular pipe findings compare with results for film flow over 2-D planar step down topography (Bontozoglou & Serifi 2008) in revealing the importance of flow rate in determining whether a capillary ridge or a series of capillary waves forms, as this is

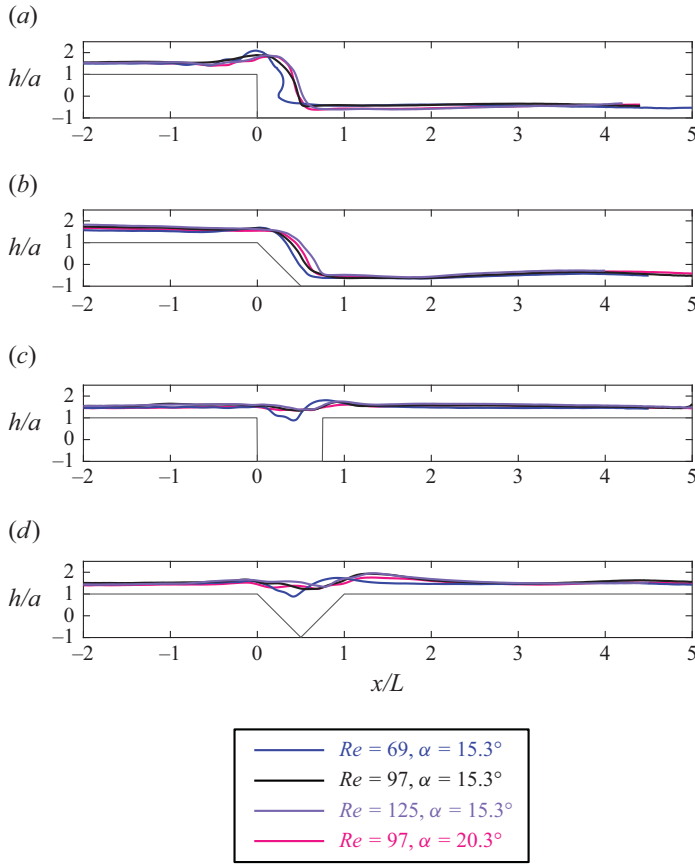


Figure 6. Time-averaged absolute free surface elevation normalized by substrate amplitude for (a) RSD, (b) TSD, (c) RTR and (d) TTR topographies. Data are replicated in figure 7 with increased magnification for clarity. Substrate topography is shown as a grey line. Uncertainty in substrate location is approximately  $0.08a$ , and in absolute free surface elevation is approximately  $0.02a$ .

indicative of the balance between inertia and surface tension effects. The capillary ridge is often the most prominent feature of film flow response over isolated 2-D planar topography (Fernandez Parent *et al.* 1998; Aksel 2000; Kalliadasis *et al.* 2000; Mazouchi & Homsy 2001; Decré & Baret 2003; Gaskell *et al.* 2004b; Davis & Troian 2005; Bontozoglou & Serifi 2008; Pal *et al.* 2022), whereas for the current results, the capillary ridge has a reduced relative prominence. The reduced prominence is likely due to the circumferential extent of the water either at the bottom of a step or within a trough, resulting in the water travelling through regions of considerably different spanwise extent in circular pipes, as opposed to planar cases that have a consistent width.

The series of capillary waves preceding the capillary ridge has been observed in steady-state film flows over planar step down topography (Mazouchi & Homsy 2001; Bontozoglou & Serifi 2008) or planar troughs (Pal *et al.* 2021). For the circular pipe RSD cases in figure 7(a) of  $Re = 125$  and  $\alpha = 15.3^\circ$  and  $Re = 97$  and  $\alpha = 20.3^\circ$ , the capillary waves do not descend significantly in the radial direction before rising towards the next capillary crest, in contrast to the case for  $Re = 69$  and  $\alpha = 15.3^\circ$ , which produces more well-defined capillary waves that better compare to planar cases. For the intermediate flow rate  $Re = 97$  and  $\alpha = 15.3^\circ$ , the flow rises monotonically to a maximum elevation before descending

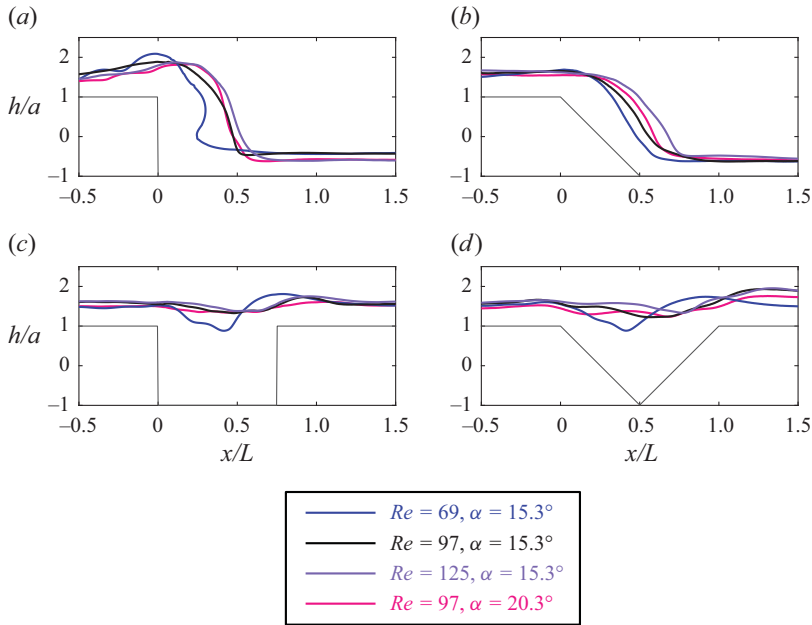


Figure 7. Time-averaged absolute free surface elevation normalized by substrate amplitude for (a) RSD, (b) TSD, (c) RTR and (d) TTR topographies. Data are identical to those shown in figure 6, with increased magnification to improve clarity. Substrate topography is shown as a grey line. Uncertainty in substrate location is approximately  $0.08a$ , and in absolute free surface elevation is approximately  $0.02a$ .

after the step; hence the angle of inclination influences the development of a capillary ridge similar to the film flow response to 2-D planar step down topography (Aksel 2000). For the highest two flow rates, the film descends approximately monotonically; however, for the lowest flow rate, the free surface forms a capillary wave that transitions into a sustained overhang over the film that forms the outlet to the topography. This steady overhang is distinct from any free surface observed for film flow over 2-D step down or 3-D rectangular trough planar topography (Aksel 2000; Kalliadasis *et al.* 2000; Mazouchi & Homsy 2001; Bielarz & Kalliadasis 2003; Decré & Baret 2003; Davis & Troian 2005; Bontozoglou & Serifi 2008; Veremieiev *et al.* 2010; Scholle *et al.* 2019; Pal *et al.* 2022). As noted in § 2.2, the c.d.f.-based edge-detection method applied to the instantaneous images was sensitive only to radial variations in intensity, so for the flow condition that generated an overhang, the portion of the image that included axial variations in intensity was separated so the c.d.f.-based method could be applied in the axial direction.

The only phenomenon similar to the steady overhang produced by the RSD topography, as seen in figures 6(a) and 7(a) at the lowest flow rate, is that found within the examination of moving contact lines over topography. As the contact line spreads, a capillary ridge forms at the leading edge for some flow conditions. As the leading edge encounters 2-D planar topography, a subsequent bulge of fluid forms on the downstream face of the topography, and builds in volume before it either reaches the next face of the substrate or detaches and drips (Gramlich *et al.* 2004; Mazloomi & Moosavi 2012, 2013; Lampropoulos *et al.* 2016; Karapetsas *et al.* 2017; Singh & Tiwari 2024). For some conditions, this bulge of fluid develops a pressure gradient large enough to drive the film towards the bottom corner of the step (Gramlich *et al.* 2004; Lampropoulos *et al.* 2016). While the free surface shape of the film in figures 6(a) and 7(a) for  $Re = 69$  is similar to the developing bulge in some moving contact line observations, a moving contact line

encounters a clean surface, whereas the film flow in the current study proceeds over a previously wet surface. Therefore, this indirect comparison is made with caution, as the adhesion that is partly responsible for the bulge formation within a moving contact line over topography is not likely to be an effect present in the steady overhang detected in the current film flow results. The curvature of the steady overhang in [figure 7\(a\)](#) would produce a pressure difference between the largest axial extent of the overhang near  $h/a = 0.8$  and the subsequent minimum axial extent near  $h/a = 0$ . Therefore, the steady overhang could form in response to the preceding capillary ridge existing over the edge of the step rather than further upstream as observed for planar cases, indicating that inertia caused the surface tension effects to develop further downstream as the Reynolds number increases from 69 to 97, and again to 125. The curvature of the steady overhang and the resulting surface pressure gradient forces the water closer to the step face, similar to the bulge in spreading contact lines such that the axial distance between the free surface and the step face is reduced. For higher flow rates, the inertia becomes dominant and forces capillary effects to be imposed entirely on top of the volume of water at the base of the step, and no bulge forms to bring the free surface closer to the step face.

For the TSD, RTR and TTR topographies, shown in [figures 7\(b\), 7\(c\), and 7\(d\)](#), capillary wave patterns are less well developed upstream of the topography. The TSD topography ([figure 7b](#)) produces a time-averaged response that primarily aligns with the topography shape, with only minor evidence of capillary waves at the lowest flow rate. A comparison of film response between TSD ([figure 7b](#)) and RSD ([figure 7a](#)) topographies demonstrates that a capillary ridge is needed to turn the flow  $90^\circ$  over the RSD topography (Mazouchi & Homsy 2001), but not for the  $45^\circ$  turn over the TSD topography. The fact that the triangular topographies produce a reduced steady-state effect compared to their rectangular counterparts is in contrast to the results for corrugated circular pipes, for which the triangular topography generated some of the most distinct patterns in the time-averaged free surface (Kuehner 2022), highlighting that similarities and differences exist between the responses to isolated topography and corrugations.

For both single-trough topographies ([figures 7c,d](#)), the film descends further within the trough and closer to the upstream wall of the topography for the lowest flow rate, the only flow condition for which the film height falls below  $h/a = 1$ . Similar to the lowest flow rate for the RSD topography that developed the steady overhang, the lowest flow rate over the trough topographies allows surface tension effects to take hold ahead of the topography, and causes the capillary ridge at the leading edge of the trough to have a longer axial extent. This capillary ridge at low flow rate can force the film further into the trough and closer to the upstream trough face, similar to the observations over RSD topography. At higher flow rates, inertia dominates and surface tension effects are unable to draw the free surface into the trough or as close to the upstream topography face as occurred for the lowest flow rate case. There are similarities in the shape of the free surface between these two different trough topographies when comparing individual cases of flow rate and angle of inclination in [figures 7\(c\) and 7\(d\)](#), indicating that the flow rate and angle of inclination have a stronger effect than the shape of the topography for these cases. The similar magnitude of free surface response compares well with the results found for corrugated circular pipes, for which rectangular corrugations with this trough length produced a statically deformed free surface amplitude similar to that for triangular corrugations (Kuehner 2022).

For all flow conditions in trough substrates, the free surface responds to the trough by decreasing elevation over the trough before rising through a capillary ridge that forms at the outlet of the trough. The capillary ridge at the trough outlet is also found in film flow over 2-D planar step up topography (Bontozoglou & Serifi 2008), but not in film flow over a 2-D planar rectangular trough (Kalliadasis *et al.* 2000; Mazouchi & Homsy 2001; Decré

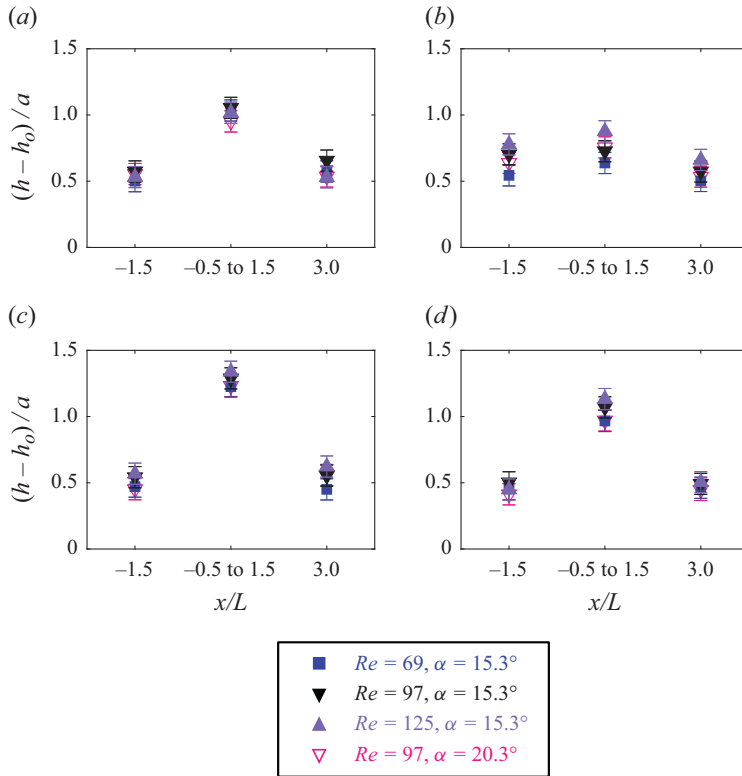


Figure 8. Time-averaged film thickness normalized by substrate amplitude at  $x/L = -1.5$ , spatially averaged over  $x/L = -0.5$  to  $x/L = 1.5$ , and at  $x/L = 3.0$  for (a) RSD, (b) TSD, (c) RTR and (d) TTR topographies.

& Baret 2003; Gaskell *et al.* 2004b; Pal *et al.* 2021, 2022). A similar capillary ridge forms at the outlet of 3-D rectangular troughs (Decré & Baret 2003; Gaskell *et al.* 2004b; Pal *et al.* 2021); hence the 3-D planar rectangular trough cases are closer comparisons to the circular pipe cases, further indicating the importance of the variable spanwise width of the film in circular pipes with topography as discussed above.

To further investigate the time-averaged free surface dependence on flow rate, inclination angle and topography shape, figure 8 displays the time-averaged film thickness  $h - h_o$  normalized by the amplitude of the topography within three axial ranges. The first axial location is upstream of the topography at  $x/L = -1.5$ , the next represents a spatial average over the axial region in the vicinity of the isolated topography defined by  $x/L = -0.5$  to  $x/L = 1.5$ , and the final axial location is downstream of the topography at  $x/L = 3.0$ . In general, the time-averaged film thickness increases with flow rate and decreases with angle of inclination, most notably for the TSD topography in figure 8(b). The increase in film thickness with flow rate aligns with the findings in corrugated circular pipes (Kuehner 2022), and the trends compare well with the expectations that a higher flow rate should increase the volume of water and average thickness in the pipe, and a larger angle of inclination should increase average film velocity, leading to a reduction in film thickness to maintain volume flow rate. Comparing variations between topography shapes, the TSD topography provides a substantially different film response than the other three shapes, as it produces a film thickness that is larger upstream and downstream of the trough, while a reduced film thickness during the interaction with the trough is reflective of the reduced turning associated with the TSD topography, which diminishes

the surface tension effects in the vicinity of the topography. For all topographies, however, the film thickness is always larger in the vicinity of the topography than before or after, due to the capillary effects that lead to increased curvature at the free surface, such as through a capillary ridge or series of capillary waves. Although there are notable variations in free surface curvature with changes in flow rate or inclination angle in the vicinity of the topography, as highlighted in [figure 7](#), the average film thickness in this axial region is relatively similar across flow conditions within a particular topography, further indicating the effect of the circumferential extent of the water near the bottom corner of the step or within the trough, which affords consistency to the volume of water near the topography between the flow conditions examined. The effect of the final downstream rise discussed above is also evident in [figure 8](#) as a difference in film thickness from upstream at  $x/L = -1.5$  to downstream at  $x/L = 3$ . While this downstream rise makes it appear that the topography would have a permanent effect on the downstream thickness, and therefore width, of the film flow in the circular pipe, for the cases in which the end of the downstream rise can be observed, such as for  $Re = 69$  for the RSD topography in [figure 6\(a\)](#), the film thickness returns to approximately the same as that upstream of topography. In addition, small variations in film thickness from upstream to downstream of the step topographies can be attributed to the difference in pipe diameter from 47 mm upstream to 54.6 mm downstream of the step, which will produce different surface tension effects in the spanwise direction.

As mentioned above, the capillary ridge that forms near the beginning of the topography compares to that observed for film flow over similar 2-D and 3-D planar topography; however, for some flow conditions, the location of the capillary ridge in the circular pipe is further downstream than that found over planar substrates. The location of all identifiable capillary ridges in the time-averaged free surface are presented in [figure 9](#). For many cases, the capillary ridge exists just prior to or beyond the topography onset, in direct contrast to film flow over 2-D and 3-D planar topography, which always produces a capillary ridge upstream of the start of the substrate topography (Kalliadasis *et al.* 2000; Gaskell *et al.* 2004b; Bontozoglou & Serifi 2008). The only exception is for the TTR topography, for which the capillary ridge is always upstream of the onset of topography. The TTR topography imposes less turning than the RTR topography, allowing the film behaviour to be more similar to that of the planar case. For the RSD, RTR and TTR topographies, the interaction between the surface tension, the axial inertia and the circumferential spreading of the film results in capillary ridge placement in contrast to that observed in planar cases. While absolute location of the capillary ridge is in disagreement with planar findings, the variation in relative location of the capillary ridge for the RSD topography is in better agreement with planar film flows for which the capillary ridge moves downstream with increasing Reynolds number (Bontozoglou & Serifi 2008) and increasing inclination angle (Aksel 2000). The RTR and TTR topographies develop contrasting trends to the RSD topography, further demonstrating the influence of the trough shape.

To highlight the variation in capillary features presented in [figures 6](#) and [7](#), the characteristics of the capillary features are investigated further. [Figure 10](#) displays the elevation of the capillary ridge, which is strongly influenced by topography shape and inclination angle, although to a lesser degree by flow rate. As expected, the sharp corner of the RSD topography produces the tallest capillary ridge to provide the favourable pressure gradient needed to flow around the  $90^\circ$  corner, whereas the smallest capillary ridge forms for the RTR topography. While the average film thickness is larger for the RTR topography in comparison to the TTR topography, as seen in [figure 8](#), it is only slightly different, and the capillary ridge elevation in [figure 10](#) is only slightly different for

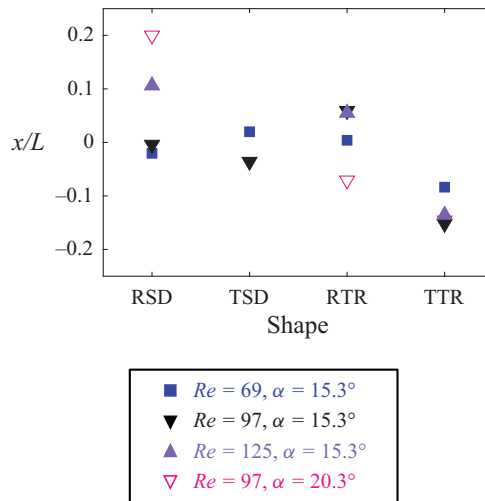


Figure 9. The dependence of the axial location of the capillary ridge normalized by  $L$  on topography shape. Uncertainty is approximately  $0.005L$ , which is smaller than the resolution of the figure so uncertainty bars are omitted for clarity.

trough topographies. These findings imply the formation of eddies in the RTR trough that would reduce the effect of the sharp turns and result in similar behaviour of the film over the RTR and TTR topographies (Scholle *et al.* 2019). However, as the two troughs have different lengths, there are several reasons to consider for the similarities and differences between the responses to RTR and TTR topographies, and conclusions cannot be made without additional data obtained within the film flow. To examine whether the prominence of the capillary ridge might be influenced by the upstream film thickness, figure 11 presents the dependence of the capillary ridge elevation on the film thickness as measured at  $x/L = -1.5$ . While there are positive trends between capillary ridge elevation and the upstream film thickness for the RTR and TTR topographies, overall the dependence on topography shape seems to be a stronger factor in determining capillary ridge elevation.

For the flow conditions that produced a series of capillary waves prior to the topography, the axial spacing between successive capillary waves up to and including the capillary ridge is presented in figure 12, with each spacing plotted at the axial midpoint between the two wave crests. The TSD topography did not produce a series of capillary waves regardless of flow condition, so data are not included for that shape. The trough topographies also produced capillary waves downstream of the capillary ridge, and those will be analysed and discussed below when examining the transient response of the free surface. For a majority of the waves that exist prior to the onset of topography, the axial spacing between crests is in the range  $x/L = 0.3$  to  $x/L = 0.35$ , which is approximately half of the axial capillary length presented in table 1. Figure 12 reveals that the lowest flow rate for each topography produces a free surface with the longest series of capillary waves, again pointing to the balance between inertial and surface tension effects for the lowest flow rate. In a previous study of film flow over 2-D planar topography, the axial length of the capillary ridge was estimated in the range 5–10 times the Nusselt thickness (Bontozoglou & Serifi 2008), which compares well with the axial length of the capillary waves evident in figure 7 and analysed in figure 12 when considering the Nusselt thickness presented in table 1.

A characteristic length scale was investigated for the axial spacing presented in figure 12 based upon that proposed for planar film flow over step down topography (Kalliadasis

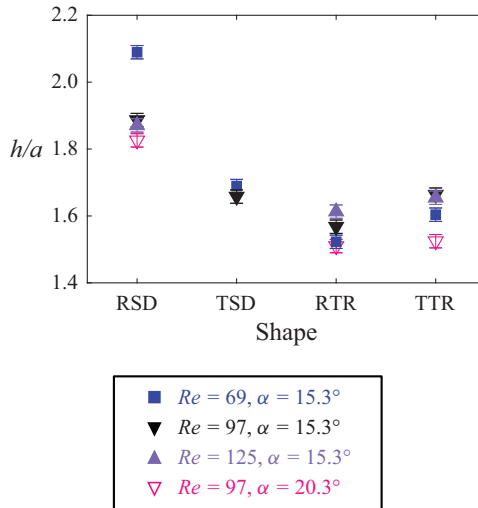


Figure 10. The dependence of the absolute free surface elevation of the capillary ridge normalized by substrate amplitude on topography shape.

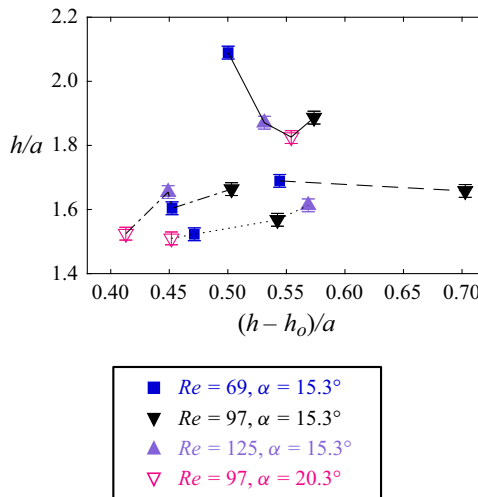


Figure 11. The dependence of the absolute capillary ridge elevation normalized by substrate amplitude on upstream film thickness measured at  $x/L = -1.5$ . Substrate topography is indicated by line type: RSD (solid), TSD (dashed), RTR (dotted) and TTR (dash-dotted).

*et al.* 2000; Mazouchi & Homay 2001; Bontozoglou & Serifi 2008). When inertia is negligible, the capillary wavelength was found to be  $h_N/Ca^{1/3}$ , where  $Ca$  is the capillary number defined as  $Ca = \rho g h_N^2 / \sigma$  for gravity-driven film flow (Kalliadasis *et al.* 2000; Mazouchi & Homay 2001). As the Reynolds number increases and the effects of inertia become stronger, the capillary wavelength is predicted to change to either  $h_N/(Re Ca)^{1/2}$  or  $h_N/Ca^{1/2}$  (Bontozoglou & Serifi 2008). Previous work in film flow over planar corrugated plates (Trifonov 2007; Nguyen & Bontozoglou 2011) and within corrugated pipes (Kuehner *et al.* 2019, 2021; Kuehner 2022) has utilized the capillary wavelength of  $h_N/Ca^{1/2}$  when effects of inertia are significant, which results in the capillary length scale relations presented in table 1. All three scaling arguments were applied to the data in

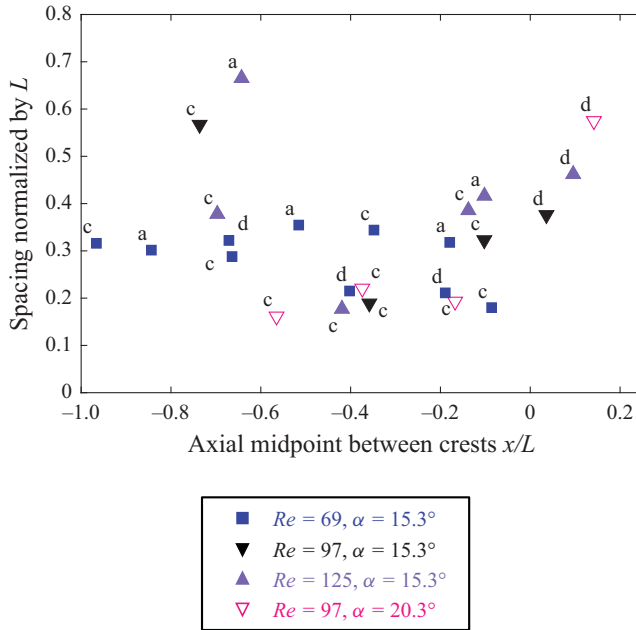


Figure 12. Axial spacing normalized by  $L$  between successive capillary crests up to and including the capillary ridge. Substrate topography is indicated by the letter next to each marker: a – RSD, c – RTR and d – TTR. Uncertainty is approximately  $0.005L$ , which is smaller than the resolution of the figure so uncertainty bars are omitted for clarity.

figure 12 using the predicted Nusselt thickness for film flow over an inclined plate, as well as using the actual film thickness measured upstream of the topography at  $x/L = -1.5$ ; however, none of the length scales collapsed the findings, in particular for the capillary waves that exist near or downstream of the onset of the topography for which there is greater dispersion in the data. The incompatibility of the planar scaling for the axial spacing of capillary waves in circular pipes can be attributed to the additional factors that are not present in the planar cases. In particular, the surface tension effects and non-uniform depth of the film in the lateral direction significantly impact the development of the film flow upstream of, within, and downstream of the topography. While attempts at scaling are limited without data in the lateral plane, the findings in figure 12 reveal that there might be three different capillary wave modes: a short wave mode for the axial spacing grouped within  $x/L \approx 0.15$  and  $x/L \approx 0.25$ , a second short wave mode for the axial spacing grouped within  $x/L \approx 0.3$  and  $x/L \approx 0.4$ , and a longer wave mode for the axial spacing exceeding  $x/L = 0.5$ . Previous studies of film flow over planar corrugated plates have revealed the existence of short and long wave modes (Plumerault *et al.* 2010; Cao *et al.* 2013). Before characteristic length scales can be determined, further observations of the film flow behaviour in the spanwise direction is needed to understand the ways in which the spanwise extent of the film impacts the axial spacing of capillary waves, and whether these different modes exist.

### 3.2. Transient free surface response

As one motivation for the current work was to investigate whether there are elements of the film flow over isolated topography that might lead to or contribute to the periodic flow in corrugated circular pipes, we examine the transient free surface response to isolated topography. There are no similar reports on transient response in film flow over 2-D or

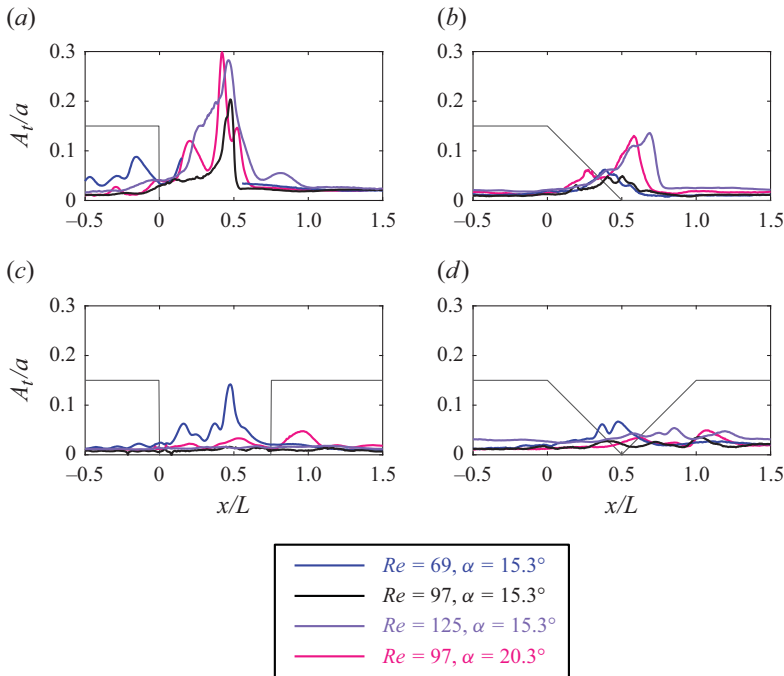


Figure 13. Amplitude of transient free surface fluctuations normalized by substrate amplitude for (a) RSD, (b) TSD, (c) RTR and (d) TTR topographies. Substrate topography is plotted over a radial scale different from  $A_f/a$ . Uncertainty in amplitude of transient free surface fluctuations is approximately  $0.02a$ .

3-D planar isolated topography, so comparisons will be limited to previous film flow studies in corrugated circular pipes. To estimate the transient free surface response, the root mean square amplitude of the time series of free surface elevation in the radial direction is calculated at each point along the free surface to provide a measure of the peak amplitude  $A_f$  of the transient free surface fluctuations, similar to the methods applied previously (Kuehner *et al.* 2021; Kuehner 2022). The axial distribution of the peak amplitude normalized by the amplitude of the substrate is presented in figure 13 over the axial region in the vicinity of the isolated topography. The measurement uncertainty for peak amplitude is estimated as the uncertainty of a length taken from an image, or  $0.02a$ . As the peak amplitude in advance of and downstream of the topography outside of the axial limits of figure 13 is at or below the uncertainty, the transient fluctuations are considered negligible in those regions. The gap in the profile for the lowest flow rate  $Re = 69$  in figure 13(a) will be discussed further below in relation to the steady overhang. For the step down topographies in figures 13(a) and 13(b), the peak amplitude rises to a maximum in the region near  $x/L = 0.5$  where the time-averaged free surface slows its descent and turns back towards the axial centreline to flow along the outer radius of the pipe, which aligns with an inflection point of the descending time-averaged free surface. This inflection point in the free surface would impose an adverse pressure gradient from low surface pressure to high surface pressure that could destabilize the flow and produce the resulting free surface fluctuations.

For the trough topographies in figures 13(c) and 13(d), the peak amplitude reaches a maximum near the middle of the trough for the lowest flow rate, and just after the trough ends for the higher flow rates. Comparing with the time-averaged free surface profiles in figures 7(c) and 7(d), the maxima in figures 13(c) and 13(d) are seen to be just upstream

of the location of the capillary ridge that forms as the film rises over the outlet of the trough, again near an inflection point in the time-averaged free surface. The capillary ridge at the exit of the trough imposes an adverse pressure gradient from the low free surface pressure at the lowest upstream elevation to the high free surface pressure at the top of this capillary ridge. For the trough topographies, except for the largest inclination angle for the RTR topography, the axial profile of peak amplitude displays additional local maxima at approximately half the spacing of the capillary waves observable over the entire trough region in figures 7(c) or 7(d). This spacing is approximately half of that documented in figure 12 for many of the capillary waves upstream of the capillary ridge. In comparing the axial location of the local maxima in figures 13(c) and 13(d) to the free surface elevations in figures 7(c) and 7(d), most clearly delineated by the lowest flow rate, the local maxima in peak amplitude of transient free surface fluctuations align with inflection points of the time-averaged free surface elevation at the rise and fall of the series of capillary waves downstream of the entrance to the topography. Similar to the inflection point in the free surface discussed above for the RSD and TSD topographies, and the inflection point prior to the capillary ridge at the exit of the trough, the inflection points in the free surface associated with the crests of capillary waves over the troughs are related to the development of adverse pressure gradients along the free surface. Hence these adverse pressure gradients might lead to the destabilization of the flow at these locations and free surface fluctuations. These axial locations of peak transient amplitude for isolated topography are in contrast to the axial locations of maxima found for the film flow over corrugated circular pipes, which occurred at the location of minimum elevation of the time-averaged free surface rather than at inflection points (Kuehner *et al.* 2019, 2021; Kuehner 2022). At the highest flow rate and largest inclination angle for the RSD topography, seen in figure 13(a), there is a rise in the amplitude of transient free surface fluctuations at approximately  $x/L = 0.25$ . This increase in transient behaviour does not correspond to an inflection point in the time-averaged free surface as found for all other local maxima, and is indicative of a different unsteady free surface behaviour discussed further below.

A review of the time series of instantaneous images reveals that the unsteady behaviour evident in figure 13 is often detectable as a transient axial shift in the location of depressions prior to capillary waves combined with a transient variation in amplitude of the depressions. An example of these trends is provided in figure 14 for the film flow over RTR topography for  $Re = 69$  and  $\alpha = 15.3^\circ$ . There is minimal variation in free surface elevation upstream or downstream of the topography over the time interval presented. As indicated by the amplitude of transient free surface fluctuations, also included in figure 14, the free surface curvature varies in time most notably over the trough. The depression in the free surface near  $x/L = 0.5$  ahead of the capillary ridge at the exit of the topography moves downstream over 0.04 s, then moves further downstream and decreases in elevation over the next 0.04 s. The two peaks in the amplitude of transient free surface fluctuations associated with the movement of this depression align with the furthest upstream and downstream locations of this particular depression over the course of the data set. The peak in transient free surface fluctuations near  $x/L = 0.5$  has a larger magnitude than that near  $x/L = 0.35$  because the elevation of the depression varies more significantly near  $x/L = 0.5$ , whereas the depression primarily moves axially at the farthest upstream location near  $x/L = 0.35$ . Depressions in the free surface such as these are associated with locally low pressure at the free surface due to surface tension effects, and these lower-pressure regions move axially and vary in elevation to a larger extent when compared to the high pressure region just downstream at the top of the next capillary wave. Hence the relatively high pressure at the peaks of capillary waves provides more stable flow

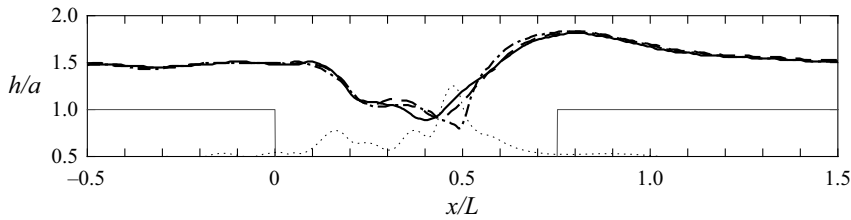


Figure 14. Instantaneous absolute free surface elevation normalized by substrate amplitude for RTR topography,  $Re = 69$  and  $\alpha = 15.3^\circ$  at  $t_o$  (solid line),  $t_o + 0.04$  s (dashed line) and  $t_o + 0.08$  s (dash-dotted line). A three-point moving average is applied to absolute free surface elevation data to improve clarity. The amplitude of transient free surface fluctuations normalized by substrate amplitude from figure 13(a) is plotted on a different radial scale for comparison (dotted line). Substrate topography is shown as a grey line. Uncertainty in substrate location is approximately  $0.08a$ , and in absolute free surface elevation is approximately  $0.02a$ .

features, in both magnitude and location, compared to the low-pressure regions in the depressions. Further upstream in the trough near  $x/L = 0.15$  and  $x/L = 0.25$ , the peaks in the amplitude of transient free surface fluctuations correspond to the axial motion of the depression between the capillary ridge at the entrance to the topography and the smaller capillary peak that resides near the middle of the trough; however, for the instantaneous sequence presented in figure 14, this depression does not move as significantly as the depression near  $x/L = 0.35$  to  $x/L = 0.5$ .

The gap in the amplitude of transient free surface fluctuations within the axial range  $x/L = 0.15$  to  $x/L = 0.55$  for  $Re = 69$  for the RSD topography in figure 13(a) relates to the overhang in the time-averaged free surface profile. To account for the overhang, the method of determining the transient amplitude in this region had to be modified. In the region near the overhang, the transient free surface is captured as a fluctuation in the axial direction instead of the radial direction that is used at all other locations. Figure 15 presents the radial variation in the amplitude of transient free surface fluctuations for the region of the time-averaged free surface associated with the overhang. The magnitude of the transient free surface fluctuations in this region is similar to that produced elsewhere at these flow conditions, as presented in figure 13(a), and rises to a maximum near the sharp curvature in the time-averaged free surface profile in a manner similar to the correspondence between local maxima and inflection points elsewhere in the free surface. If the steady overhang is considered to form in response to the film flow extending further past the step face than it would in a planar flow, then the high pressure that would exist at the axial peak of the steady overhang near  $h/a = 0.8$  would be followed by a lower surface pressure in the sharp curvature of the portion of the film that recedes axially towards the step face near  $h/a = 0$ . This low-pressure region is susceptible to disturbance, leading to the increase in transient free surface fluctuations in this region.

To determine the effect of flow condition and topography on the peak amplitude of the transient free surface fluctuations, the maximum amplitude  $A_{t,max}$  for each flow condition and topography is presented in figure 16. The maximum amplitude produced in circular pipes with isolated topography is approximately half of the maximum observed in corrugated circular pipes (Kuehner 2022). This comparison aligns with the expectations that the periodic travelling waves in film flows over corrugations arise due to a resonance (Plumerault *et al.* 2010); hence the film response to corrugations would be expected to be of larger magnitude than that for isolated topography. Overall, the RSD topography produces the largest transient free surface fluctuations, and for the step down topographies, the magnitude generally increases with flow rate and inclination angle, which corresponds

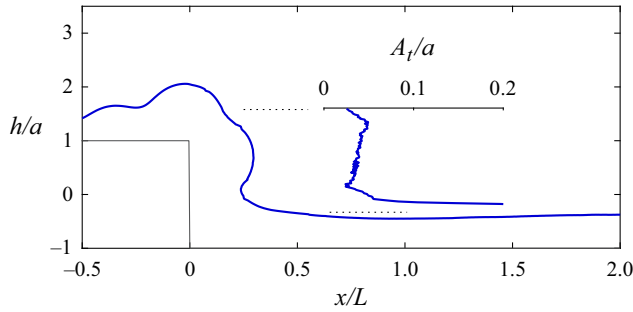


Figure 15. Amplitude of transient free surface fluctuations normalized by substrate amplitude for the radial portion of the time-averaged absolute free surface elevation for the RSD topography,  $Re = 69$  and  $\alpha = 15.3^\circ$ . Time-averaged absolute free surface elevation and substrate topography, shown as a grey line, are plotted over an axial scale different from  $A_t/a$ . Uncertainty in amplitude of transient free surface fluctuations is approximately  $0.02a$ .

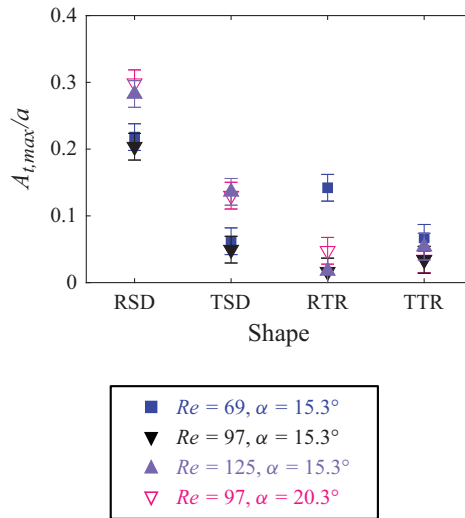


Figure 16. The dependence of maximum amplitude of transient free surface fluctuations normalized by substrate amplitude on topography shape.

with increased kinetic energy entering the topography and leading to larger free surface fluctuations. In previous work, triangular corrugations generated larger peak amplitudes than rectangular corrugations (Kuehner 2022); however, the enhanced importance of capillary features caused by the isolated turns in the current substrates compared to the corrugated circular pipes leads to the isolated RSD topography producing larger features with larger transient fluctuations than the isolated TSD topography.

As noted above in reference to figure 13(a) for the cases  $Re = 125$ ,  $\alpha = 15.3^\circ$  and  $Re = 97$ ,  $\alpha = 20.3^\circ$ , there is a rise in the amplitude of transient free surface fluctuations near  $x/L = 0.25$ . During the data collection process, it was noted that for brief moments in time, an extra ridge of fluid would develop on top of the capillary ridge. The extra ridge was a small feature but observable by eye. Figure 17 displays example fluorescence images for the highest flow rate case presented on a logarithmic scale for fluorescence intensity to add clarity. The images include the location of the substrate topography (red line) and the time-averaged free surface profile (purple line) from figure 6(a) for reference. The extra ridge

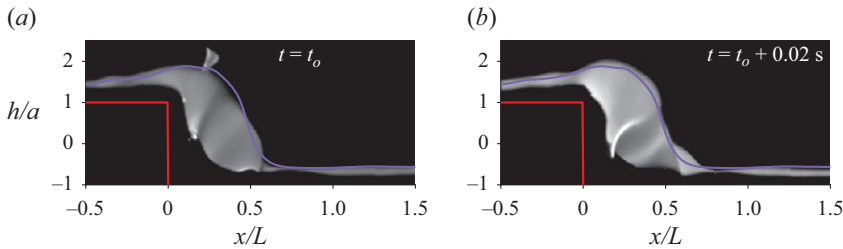


Figure 17. Instantaneous fluorescence images of film flow over RSD topography for  $Re = 125$ ,  $\alpha = 15.3^\circ$ , with (a) extra ridge evident and (b) extra ridge not evident. Image intensity is plotted on a logarithmic scale for clarity. The red line indicates the approximated location of the substrate, and the purple line represents the time-averaged free surface profile presented in figures 6 and 7. The fluorescence within the volume of the film is viewed through the non-uniform free surface, causing a distortion that makes the bottom of the water appear detached from the substrate.

is observed at  $x/L = 0.25$  as an elevation above the time-averaged free surface profile. As displayed in figure 17(a), due to the small radius of curvature for this extra ridge, the shape of the fluorescence captured within the extra ridge is highly distorted even though visual observations of the phenomenon indicated that the extra ridge has curvature similar to the capillary ridge with a shorter axial extent. As noted in § 2.2, the appearance of the extra ridge required a modification to the c.d.f.-based method of edge detection to include a hybrid Canny approach for these two data sets. To our knowledge, there is no comparable phenomenon to this extra ridge observed in film flow over 2-D or 3-D planar topography. The limited temporal scale of these occurrences is highlighted by the time difference between the images in figures 17(a) and 17(b), when the extra ridge has disappeared. These are sequential images from the same time series, hence the time separation is 0.02 seconds. As further evidence that this extra ridge is an infrequent occurrence, the time-averaged free surface response is primarily unaffected by the occasional addition of the extra ridge elevation.

As capillary waves, and in particular, the capillary ridge at the entrance to the topography, form to develop a pressure gradient to turn the flow and maintain contact with the downstream face of the step, this extra ridge atop the capillary ridge likely forms for similar reason. Considering that the extra ridge forms only for flow conditions that produce a capillary ridge beyond the onset of topography, the capillary ridge exists atop a volume of fluid that would not be present in a similar planar case. The extra ridge would develop an increased free surface pressure at its peak above that which would occur at the top of the capillary ridge alone, forcing the flow to turn downwards further upstream than it otherwise would. Evidence of this effect is displayed in figure 17(a), as the film just downstream of the extra ridge is turned downwards ahead of the time-averaged free surface location; whereas in figure 17(b), the free surface extends beyond the time-averaged free surface location both near the end of the capillary ridge near  $h/a = 1.5$  and as the free surface turns away from the topography near  $h/a = -0.5$ .

The extra ridge for the case  $Re = 125$  and  $\alpha = 15.3^\circ$  presented in figure 17 tended to have large relative elevation. For example, the extra ridge in figure 17(a) has an elevation above the capillary ridge that is approximately equivalent to the elevation of the capillary ridge above the upstream incoming film thickness. A wider range of behaviour was observed for the case  $Re = 97$  and  $\alpha = 20.3^\circ$  displayed in figure 18, where the intensity is again presented on a logarithmic scale, and the time-averaged free surface profile from figure 6(a) is shown in pink. Similar to the previous case, the flow conditions in figure 18 produce a capillary ridge that is downstream of the onset of topography. For the

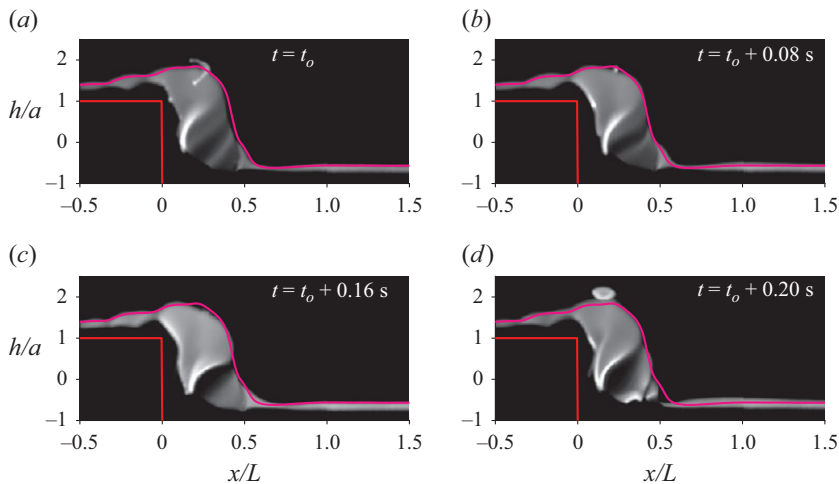


Figure 18. Instantaneous fluorescence images of film flow over RSD topography for  $Re = 97$ ,  $\alpha = 20.3^\circ$ , with (a,b,d) extra ridge evident, and (c) extra ridge not evident. Image intensity is plotted on a logarithmic scale for clarity. The red line indicates the approximated location of the substrate, and the pink line represents the time-averaged free surface profile presented in figures 6 and 7. The fluorescence within the volume of the film is viewed through the non-uniform free surface, causing a distortion that makes the bottom of the water appear detached from the substrate.

largest inclination angle, the elevation of the extra ridge was less often pronounced and instead expanded over a longer axial range than for  $Re = 125$  and  $\alpha = 15.3^\circ$ . As seen in figure 18(a), the broad extra ridge reduced to a smaller extra ridge in figure 18(b) within 0.08 s, before disappearing 0.08 s later in figure 18(c), only to reappear wider and further upstream 0.04 s later in figure 18(d). Careful examination of the free surface of the downward slope following the capillary ridge reveals that the appearance of the extra ridge might coincide with variations in the number of capillary undulations along the free surface downstream of the capillary ridge. For example, in figure 18(a), the free surface includes more undulations on the downward slope when the extra ridge is present, in comparison to figure 18(c) when the extra ridge is absent. Similar but to a lesser degree than the previous case in figure 17, the falling edge of the capillary ridge is upstream of the time-averaged free surface when the extra ridge is present, as seen in figures 18(a) and 18(d), as compared to figure 18(c) when the extra ridge is missing. As there is a considerable range of spatial behaviour within a short time scale, and as there is no known comparison to this phenomenon in film flow over similar planar topography, the behaviour of this extra ridge merits additional attention to further characterize the conditions for which it occurs, to examine the transient behaviour, and to possibly identify the impetus for its formation.

As performed for previous film flows in corrugated circular pipes (Kuehner *et al.* 2019, 2021; Kuehner 2022), a frequency analysis was applied to the transient free surface behaviour. However, in contrast to the periodicity that was evident in the film flow in corrugated circular pipes for all flow conditions and topographies, there were no cases of isolated topography that produced an indication of periodic behaviour in the range of frequencies examined, up to 25 Hz, even for those flow conditions that produced the extra ridge of fluid. Hence the variations in the capillary waves discussed in reference to figure 13 and observed in figure 14, and the extra ridge that generated transient free surface fluctuations shown in figures 17 and 18, were not associated with periodic behaviour. With the aim of potentially identifying substrate geometries for which periodic behaviour

emerges, we look towards a study of topographies that incorporate an intermediate geometric pattern, such as those including 2–10 troughs, to bridge the gap between these isolated topographies and the corrugated circular pipes studied previously. In addition, we plan to construct circular pipes out of optically pure materials to permit imaging of the film behaviour beneath the free surface, similar to that achieved in planar flows, which would afford a better understanding of the flow phenomena affecting the free surface behaviour.

#### 4. Conclusions

Gravity-driven film flow over isolated topography in circular pipes was investigated for a range of flow rates, inclination angles and topography shapes. The topography shapes were selected so that potential connections with the film flow response to periodic corrugations studied previously could be investigated. The time-averaged free surface of the thin film is affected by flow rate, inclination angle and topography shape, which aligns with similar effects found in film flow over corrugated circular pipes. For some flow conditions, a capillary ridge develops near the start of the topography, with a series of upstream capillary waves observed for a subset of those conditions. The capillary ridge has similar dependencies on flow rate and inclination angle as seen for film flows over 2-D and 3-D planar topography; however, the capillary ridge often forms downstream of the onset of topography in circular pipes, in contrast to the 2-D and 3-D planar cases for which the capillary ridge always precedes the topography. For the RSD topography at the lowest flow rate, a steady overhang develops along the downstream face of the topography that has no comparison in film flow over similar 2-D or 3-D planar topography. The variance between the film flow over circular pipes and that over planar cases could be linked to the circumferential spreading of water at the bottom of the step topographies or the filling of the trough topographies, which produces a substantially wider film immediately downstream of the topography compared to that upstream of the topography.

The spatially averaged, time-averaged film thickness in the vicinity of the topography is similar between cases of flow rate and angles of inclination even though the overall curvature of the time-averaged free surface profiles differs considerably. The time-averaged free surface response to the RTR topography is similar in shape and magnitude to the TTR topography, which aligns with the similarity in response to the rectangular and triangular corrugations studied previously (Kuehner 2022). The elevation of the capillary ridge depends more strongly on topography shape than flow rate or inclination angle, and for the conditions that generate a series of capillary waves upstream of the capillary ridge, the spacing of the waves is comparable to half of the capillary length in a majority of cases. The longest series of capillary waves occurs for the lowest flow rate, indicating the balance between inertial and surface tension effects. In contrast to film flow over 2-D or 3-D planar topography, the capillary waves typically do not descend in elevation before the next capillary wave forms. The axial spacing and length of the capillary waves find good comparison with previous 2-D planar film flow results (Bontozoglou & Serifi 2008).

The transient free surface response to isolated topography is negligible upstream or downstream of the isolated topography, varies with flow rate and inclination angle, and has approximately half of the magnitude found for film flow over corrugations in a circular pipe (Kuehner 2022). The axial profiles of the amplitude of transient free surface fluctuations include local maxima that occur near the inflection points found in the time-averaged free surface, which differs from that seen in film flow over corrugated circular pipes (Kuehner *et al.* 2019, 2021; Kuehner 2022). The correspondence with inflection points in the time-averaged free surface profile produces local maxima of transient free surface fluctuations that are spaced at half the wavelength of the capillary waves or approximately

half the capillary length. Examining sequential instantaneous free surface elevations near the topography reveals that the amplitude of transient free surface fluctuations is related to depressions within the instantaneous free surface moving in the axial direction and varying in elevation.

The axial profiles of the magnitude of transient free surface fluctuations for the RSD topography at the highest flow rate and largest inclination angle include a local maximum that does not correspond to an inflection point in the time-averaged free surface and instead indicates a phenomenon unique to the RSD topography. This phenomenon was discovered to be the result of an extra ridge of fluid infrequently forming on top of the capillary ridge. The extra ridge has a variable axial length and a curvature that is narrower than that observed for any other capillary feature. The extra ridge forms only for flow conditions that produce a capillary ridge that is downstream of the onset of topography. Hence the extra ridge might form to drive the film closer to the downstream face of the topography. This extra ridge finds no comparison in film flow over 2-D or 3-D topography, and merits further examination.

A frequency analysis of the transient film flow behaviour indicates a lack of periodicity anywhere within the film flow, even for the flow conditions that develop large peak magnitudes of transient free surface fluctuations or that generate the extra ridge. This lack of periodicity is expected, as the periodic travelling waves that form over corrugated circular pipes are presumed to develop from a form of resonance that is based on the corrugation spacing, a geometric repetition that does not occur for the isolated topographies studied herein. While there is no clear indication of film flow response to isolated topography that leads to the resonance over corrugations, the current results provide findings that can be studied further for a possible link to the proposed resonance. If the travelling waves in film flow over corrugated circular pipes form from a triple resonance, as posited for the travelling waves in 2-D planar film flow (Plumerault *et al.* 2010), then the spacing of capillary waves in the time-averaged free surface and the spacing of the local maxima in the axial profile of peak magnitude of transient free surface fluctuations provide two lengths that might feed into the triple resonance. Regardless of whether these distances are relevant to the resonance, the transient free surface fluctuations measured over the topography offer an ambient source of disturbance that could be magnified by the resonance in the film flow over corrugated circular pipes. This motivates further study of substrates with an intermediate sequence of troughs that might reveal a link between the current findings for isolated topography and the previous findings for corrugated circular pipes.

**Acknowledgements.** The authors would like to thank C. Compton for assistance in developing the experimental apparatus and for helpful conversations, D. Pfaff and M. Brown for their support of 3-D printing operations, T. Marçais and K. Steinert for their support of computational processing, and P. Hinely for the loan of photographic equipment. J.P.K. is grateful to E. Kuehner for continued insightful conversations.

**Funding.** This research received no specific grant from any funding agency, commercial or not-for-profit sectors.

**Declaration of interests.** The authors report no conflict of interest.

**Data availability statement.** The data that support the findings of this study are available from the corresponding author (J.P.K.) upon reasonable request.

#### REFERENCES

- ÅKESJÖ, A., GOURDON, M., JONGSMA, A. & SASIC, S. 2023 Enhancing industrial vertical falling film evaporation through modification of heat transfer surfaces – an experimental study. *Chem. Engng Process.: Process Intensification* **191**, 109456.

- AKSEL, N. 2000 Influence of the capillarity on a creeping film flow down an inclined plane with an edge. *Arch. Appl. Mech.* **70** (1–3), 81–90.
- AKSEL, N. & SCHÖRNER, M. 2018 Films over topography: from creeping flow to linear stability, theory, and experiments, a review. *Acta Mech.* **229** (4), 1453–1482.
- AL-SHAMAA, B., KAHRAMAN, T. & WIERSCHEM, A. 2023 Steady three-dimensional patterns in gravity-driven film flow down an inclined sinusoidal bottom contour. *Phys. Fluids* **35** (3), 033307.
- ARGYRIADI, K., VLACHOGIANNIS, M. & BONTOZOGLU, V. 2006 Experimental study of inclined film flow along periodic corrugations: the effect of wall steepness. *Phys. Fluids* **18** (1), 012102.
- BARET, J.C. & DECRÉ, M.M.J. 2000 Gravity driven flows over two-dimensional topographies, measurement of the free surface using phase stepped interferometry. Philips Report UR 2000/829. American Society of Mechanical Engineers (ASME).
- BAXTER, S.J., POWER, H., CLIFFE, K.A. & HIBBERD, S. 2009 Three-dimensional thin film flow over and around an obstacle on an inclined plane. *Phys. Fluids* **21** (3), 032102.
- BERTOZZI, A.L. & BRENNER, M.P. 1997 Linear stability and transient growth in driven contact lines. *Phys. Fluids* **9** (3), 530–539.
- BIELARZ, C. & KALLIADASIS, S. 2003 Time-dependent free-surface thin film flows over topography. *Phys. Fluids* **15** (9), 2512–2524.
- BLYTH, M.G. & POZRIKIDIS, C. 2006 Film flow down an inclined plane over a three-dimensional obstacle. *Phys. Fluids* **18** (5), 052104.
- BONART, H. & REPKE, J.-U. 2018 Direct numerical simulations of liquids on microstructured surfaces: analysing the fluid dynamics on packing. *Chem. Engng Trans.* **69**, 61–66.
- BONTOZOGLU, V. & SERIFI, K. 2008 Falling film flow along steep two-dimensional topography: the effect of inertia. *Intl J. Multiphase Flow* **34** (8), 734–747.
- BOUJO, E. & SELLIER, M. 2019 Pancake making and surface coating: optimal control of a gravity-driven liquid film. *Phys. Rev. Fluids* **4** (6), 064802.
- BOWMAN, C.E. 2023 Looking for future biological control agents: the comparative function of the deutosternal groove in mesostigmatid mites. *Expl Appl. Acarol.* **91** (2), 139–225.
- CAMASSA, R., MARZUOLA, J.L., OGROSKY, H.R. & SWYGERT, S. 2021 On the stability of traveling wave solutions to thin-film and long-wave models for film flows inside a tube. *Physica D* **415**, 132750.
- CAMASSA, R., MARZUOLA, J.L., OGROSKY, H.R. & VAUGHN, N. 2016 Traveling waves for a model of gravity-driven film flows in cylindrical domains. *Physica D* **333**, 254–265.
- CAMASSA, R. & OGROSKY, H.R. 2015 On viscous film flows coating the interior of a tube: thin-film and long-wave models. *J. Fluid Mech.* **772**, 569–599.
- CAO, Z., VLACHOGIANNIS, M. & BONTOZOGLU, V. 2013 Experimental evidence for a short-wave global mode in film flow along periodic corrugations. *J. Fluid Mech.* **718**, 304–320.
- COWLING, N.P., GASKELL, P.H., LEE, Y.C. & THOMPSON, H.M. 2011 Towards the efficient numerical solution of three-dimensional thin film flows on real surfaces: an evaluation of finite-difference-based schemes. *Proc. Inst. Mech. Engrs C: J. Mech. Engng Sci.* **225** (8), 1886–1902.
- CRASTER, R.V. & MATAR, O.K. 2009 Dynamics and stability of thin liquid films. *Rev. Mod. Phys.* **81** (3), 1131–1198.
- D’ALESSIO, S.J.D. 2024 Depth-integrated models for three-dimensional flow over topography. *Flow* **4**, E8.
- DAVIS, J.M. & TROIAN, S.M. 2005 Generalized linear stability of noninertial coating flows over topographical features. *Phys. Fluids* **17** (7), 072103.
- DECRÉ, M.M.J. & BARET, J.-C. 2003 Gravity-driven flows of viscous liquids over two-dimensional topographies. *J. Fluid Mech.* **487**, 147–166.
- DECRÉ, M.M.J., FERNANDEZ-PARENT, C. & LAMMERS, J.H. 1999 Flow of a gravity driven thin liquid film over one-dimensional topographies: a tripartite approach. In *Advances in Coating and Drying of Thin Films: Proceedings ECS’99; 3rd European Coating Symposium* (ed. DURST, F. & RASZILLIER, H.), pp. 151–156. Shaker.
- EASTWICK, C., BERTIN, L. & JOHNSON, G. 2006 The effect of obstacles in a liquid film. In *ASME Turbo Expo 2006: Power for Land, Sea and Air GT2006-90520*, pp. 1–10. American Society of Mechanical Engineers (ASME).
- EASTWICK, C., HUEBNER, K., AZZOPARDI, B., SIMMONS, K., YOUNG, C. & MORRISON, R. 2005 Film flow around bearing chamber support structures. In *ASME Turbo Expo 2005: Power for Land, Sea and Air GT2005-68905*, pp. 1–6. American Society of Mechanical Engineers (ASME).
- FERNANDEZ PARENT, C., LAMMERS, J.H. & DECRÉ, M.M.J. 1998 Flow of a gravity driven thin liquid film over one-dimensional topographies. Philips Report UR 823/98. Philips Electronics N.V.

- FLECHTMANN, C.H.W., EVANS, G.O. & MCMURTRY, J.A. 1994 Some noteworthy features of the chelicerae and subcapitulum of *Phytoseiulus longipes* Evans (Acari: Mesostigmata: Phytoseiidae), with observations on the preoral channel in the phytoseiidae. *Expl Appl. Acarol.* **18** (5), 293–299.
- GABBARD, C.T. & BOSTWICK, J.B. 2021 Asymmetric instability in thin-film flow down a fiber. *Phys. Rev. Fluids* **6** (3), 034005.
- GASKELL, P.H., JIMACK, P.K., SELIER, M. & THOMPSON, H.M. 2004a Efficient and accurate time adaptive multigrid simulations of droplet spreading. *Intl J. Numer. Meth. Fluids* **45** (11), 1161–1186.
- GASKELL, P.H., JIMACK, P.K., SELIER, M., THOMPSON, H.M. & WILSON, M.C.T. 2004b Gravity-driven flow of continuous thin liquid films on non-porous substrates with topography. *J. Fluid Mech.* **509**, 253–280.
- GASKELL, P.H., LEE, Y.C. & THOMPSON, H.M. 2010 Thin film flow over and around surface topography: a general solver for the long-wave approximation and related equations. *Comput. Model. Engng Sci.* **62** (1), 77–112.
- GASKELL, P.H., THOMPSON, H.M. & VEREMIEIEV, S. 2012 Three-dimensional gravity-driven film flow over topography: full Navier–Stokes solutions. In *European Congress on Computational Methods in Applied Sciences and Engineering (ECCOMAS)* (ed. EBERHARDSTEINER J., BÖHM H.J. & RAMMERSTORFER F.G.), pp. 1410–1420. Vienna University of Technology.
- GLASS, C.R., WALTERS, K.F.A., GASKELL, P.H., LEE, Y.C., THOMPSON, H.M., EMERSON, D.R. & GU, X.-J. 2010 Recent advances in computational fluid dynamics relevant to the modelling of pesticide flow on leaf surfaces. *Pest Manage. Sci.* **66** (1), 2–9.
- GRAMLICH, C.M., MAZOUCHI, A. & HOMSY, G.M. 2004 Time-dependent free surface Stokes flow with a moving contact line. II. Flow over wedges and trenches. *Phys. Fluids* **16** (5), 1660–1667.
- HANSEN, E.B. 1986 Free surface Stokes flow over an obstacle. In *Boundary Elements VIII, Proceedings of the 8th International Conference* (ed. TANAKA M. & BREBBIA C.A.), pp. 783–792. Springer.
- HANSEN, E.B. 1991 Stokes flow of a fluid layer over an obstacle on a tilted plane. *Math. Comput. Model.* **15** (3–5), 185–193.
- HAYES, M., O'BRIEN, S.B.G. & LAMMERS, J.H. 2000 Green's function for steady flow over a small two-dimensional topography. *Phys. Fluids* **12** (11), 2845–2858.
- HEINING, C., POLLAK, T. & SELIER, M. 2013 Flow domain identification from free surface velocity in thin inertial films. *J. Fluid Mech.* **720**, 338–356.
- HEINING, C. & SELIER, M. 2017 Flow domain identification in three-dimensional creeping flows. *Phys. Fluids* **29** (1), 012107.
- HIGDON, J.J.L. 1985 Stokes flow in arbitrary two-dimensional domains: shear flow over ridges and cavities. *J. Fluid Mech.* **159** (1), 195–226.
- HINTON, E.M., HOGG, A.J. & HUPPERT, H.E. 2019 Interaction of viscous free-surface flows with topography. *J. Fluid Mech.* **876**, 912–938.
- HINTON, E.M., HOGG, A.J. & HUPPERT, H.E. 2020a Shallow free-surface Stokes flow around a corner. *Phil. Trans. R. Soc. Lond. A* **378** (2174), 20190515.
- HINTON, E.M., HOGG, A.J. & HUPPERT, H.E. 2020b Viscous free-surface flows past cylinders. *Phys. Rev. Fluids* **5** (8), 084101.
- IYER, M., CASALINHO, J., SEIWERT, J., WATTIAU, M. & DUVAL, H. 2021 Experimental study of a liquid film flowing over a perforation. *Transp. Phenom. Fluid Mech.* **67** (11), 17363.
- JENSEN, O.E., CHINI, G.P. & KING, J.R. 2004 Thin-film flows near isolated humps and interior corners. *J. Engng Maths* **50** (2–3), 289–309.
- KALLIADASIS, S., BIELARZ, C. & HOMSY, G.M. 2000 Steady free-surface thin film flows over topography. *Phys. Fluids* **12** (8), 1889–1898.
- KALLIADASIS, S. & CHANG, H.-C. 1994 Drop formation during coating of vertical fibres. *J. Fluid Mech.* **261**, 135–168.
- KALLIADASIS, S. & HOMSY, G.M. 2001 Stability of free-surface thin-film flows over topography. *J. Fluid Mech.* **448**, 387–410.
- KALLIADASIS, S., RUYER-QUIL, C., SCHEID, B. & VELARDE, M.G. 2012 *Falling Liquid Films*. Springer-Verlag.
- KARAPETSAS, G., LAMPROPOULOS, N.K., DIMAKOPOULOS, Y. & TSAMOPOULOS, J. 2017 Transient flow of gravity-driven viscous films over 3D patterned substrates: conditions leading to Wenzel, Cassie and intermediate states. *Microfluid Nanofluid* **21** (2), 17.
- KHAYAT, R.E., KIM, K.-T. & DELOSQUER, S. 2004 Influence of inertia, topography and gravity on transient axisymmetric thin-film flow. *Intl J. Numer. Meth. Fluids* **45** (4), 391–419.
- KING, A.A., CUMMINGS, L.J., NAIRE, S. & JENSEN, O.E. 2007 Liquid film dynamics in horizontal and tilted tubes: dry spots and sliding drops. *Phys. Fluids* **19** (4), 042102.

- KLIAKHANDLER, I.L., DAVIS, S.H. & BANKOFF, S.G. 2001 Viscous beads on vertical fibre. *J. Fluid Mech.* **429**, 381–390.
- KNEER, J., EASTWICK, C., MÜLLER, A., JOHNSON, G., ROBINSON, A. & BAUER, H.-J. 2008 Experimental investigations of film flows around obstacles. In *Proceedings of ASME Turbo Expo: Power for Land, Sea and Air GT2008-50630*, pp. 1461–1470. American Society of Mechanical Engineers (ASME).
- KUEHNER, J.P. 2022 Gravity-driven film flow inside an inclined corrugated pipe: an experimental investigation of corrugation shape and tip width. *Phys. Fluids* **34** (12), 122113.
- KUEHNER, J.P., LEE, M.R., DODSON, M.M., SCHIRMER, W.R., VELA DE LA GARZA EVIA, A.F. & KUTELAK, L.O. 2021 The effect of substrate amplitude and wavelength on gravity-driven film flow inside an inclined corrugated pipe. *Phys. Fluids* **33** (11), 112105.
- KUEHNER, J.P., MITCHELL, J.D. & LEE, M.R. 2019 Experimental investigation of gravity-driven film flow inside an inclined corrugated pipe. *Phys. Fluids* **31** (12), 122104.
- KWON, C.H., KWON, H.S. & JUNG, E.G. 2023 An experimental investigation on the influence of condenser bypass area for the transient and steady-state heat-transfer performance of heat pipes. *Intl Commun. Heat Mass Trans.* **148**, 107057.
- LAMPROPOULOS, N.K., DIMAKOPOULOS, Y. & TSAMOPOULOS, J. 2016 Transient flow of gravity-driven viscous films over substrates with rectangular topographical features. *Microfluid Nanofluid* **20** (3), 51.
- LANDEL, J.R. & WILSON, D.I. 2021 The fluid mechanics of cleaning and decontamination of surfaces. *Annu. Rev. Fluid Mech.* **53** (1), 147–171.
- LEDDA, P.G., BALESTRA, G., LERISSON, G., SCHEID, B., WYART, M. & GALLAIRE, F. 2021 Hydrodynamic-driven morphogenesis of karst draperies: spatio-temporal analysis of the two-dimensional impulse response. *J. Fluid Mech.* **910**, A53.
- LEE, Y.C., THOMPSON, H.M. & GASKELL, P.H. 2007 An efficient adaptive multigrid algorithm for predicting thin film flow on surfaces containing localised topographic features. *Comput. Fluids* **36** (5), 838–855.
- LEE, Y.C., THOMPSON, H.M. & GASKELL, P.H. 2008 The efficient and accurate solution of continuous thin film flow over surface patterning and past occlusions. *Intl J. Numer. Meth. Fluids* **56** (8), 1375–1381.
- LEE, Y.C., THOMPSON, H.M. & GASKELL, P.H. 2011 Three-dimensional thin film and droplet flows over and past surface features with complex physics. *Comput. Fluids* **46** (1), 306–311.
- LEONTIDIS, V., VATTEVILLE, J., VLACHOGIANNIS, M., ANDRITSOS, N. & BONTOZOGLOU, V. 2010 Nominally two-dimensional waves in inclined film flow in channels of finite width. *Phys. Fluids* **22** (11), 112106.
- LI, S., LI, C. & WANG, W. 2022 Simulation of unsteady flows of oil/gas in the ventless bearing chamber of an aero-engine. *Aerospace* **9** (4), 211.
- LI, X., SOVILLA, B., GRAY, J.M.N.T. & GUAME, J. 2024 Transient wave activity in snow avalanches is controlled by entrainment and topography. *Commun. Earth Environ.* **5** (1), 77.
- LIN, T.-S., DIJKSMAN, J.A. & KONDIC, L. 2021 Thin liquid films in a funnel. *J. Fluid Mech.* **924**, A26.
- LISTER, J.R., RALLISON, J.M., KING, A.A., CUMMINGS, L.J. & JENSEN, O.E. 2006 Capillary drainage of an annular film: the dynamics of collars and lobes. *J. Fluid Mech.* **552**, 311–343.
- LUCÉA, M., DECRÉ, M.M.J. & LAMMERS, J.H. 1999 Flow of a gravity driven thin liquid film over topographies, a detailed comparison of theory and experiments. Philips Report UR 833/99. Koninklijke Philips Electronics N.V.
- MA, C., HU, S., DONG, G. & LI, B. 2020 Fingering instability of a gravity-driven thin film flowing down a vertical tube with wall slippage. *Appl. Sci.* **10** (1), 76.
- MAZLOOMI, A. & MOOSAVI, A. 2012 Effects of various parameters on the coating of substrates with trenches. *Adv. Mat. Res.* **569**, 219–222.
- MAZLOOMI, A. & MOOSAVI, A. 2013 Thin liquid film flow over substrates with two topographical features. *Phys. Rev. E* **87** (2), 022409.
- MAZOUCHI, A., GRAMLICH, C.M. & HOMSY, G.M. 2004 Time-dependent free surface Stokes flow with a moving contact line. I. Flow over plane surfaces. *Phys. Fluids* **16** (5), 1647–1659.
- MAZOUCHI, A. & HOMSY, G.M. 2001 Free surface Stokes flow over topography. *Phys. Fluids* **13** (10), 2751–2761.
- MEHDAOUI, H., ABDERRAHMANE, H.A., BOUDA, F.N., KOULALI, A. & HAMANI, S. 2021 2D numerical simulation of tear film dynamics: effects of shear-thinning properties. *Eur. J. Mech. B/Fluids* **90**, 128–136.
- NGUYEN, P.-K. & BONTOZOGLOU, V. 2011 Steady solutions of inertial film flow along strongly undulated substrates. *Phys. Fluids* **23** (5), 052103.
- OVCHAROVA, A.S. 2006 Leveling a capillary ridge generated by substrate geometry. *Comput. Maths Math. Phys.* **46** (2), 305–314.

- PAL, S.K., SANYASIRAJU, Y.V.S.S. & USHA, R. 2021 A consistent energy integral model for a film over a substrate featuring topographies. *Intl J. Numer. Meth. Fluids* **93** (12), 3424–3446.
- PAL, S.K., SANYASIRAJU, Y.V.S.S. & USHA, R. 2022 Investigation on the performance of meshfree RBF based method for the solution of thin film flows over topographies through depth-averaged momentum integral model. *J. Comput. Sci.* **63**, 101777.
- PETTAS, D., KARAPETSAS, G., DIMAKOPOULOS, Y. & TSAMOPOULOS, J. 2017 On the degree of wetting of a slit by a liquid film flowing along an inclined plane. *J. Fluid Mech.* **820**, 5–41.
- PEURRUNG, L.M. & GRAVES, D.B. 1991 Film thickness profiles over topography in spin coating. *J. Electrochem. Soc.* **138** (7), 2115–2124.
- PEURRUNG, L.M. & GRAVES, D.B. 1993 Spin coating over topography. *IEEE Trans. Semiconduct. Man.* **6** (1), 72–76.
- PLUMERAULT, L.-R., ASTRUC, D. & THUAL, O. 2010 High-Reynolds shallow flow over an inclined sinusoidal bottom. *Phys. Fluids* **22** (5), 054110.
- POZRIKIDIS, C. & THORODDSEN, S.T. 1991 The deformation of a liquid film flowing down an inclined plane wall over a small particle arrested on the wall. *Phys. Fluids A: Fluid Dyn.* **3** (11), 2546–2558.
- PRITCHARD, W.G., SCOTT, L.R. & TAVENER, S.J. 1992 Numerical and asymptotic methods for certain viscous free-surface flows. *Phil. Trans. R. Soc. Lond. A: Phys. Sci. Engng* **340**, 1–45.
- ROY, R.V., ROBERTS, A.J. & SIMPSON, M.E. 2002 A lubrication model of coating flows over a curved substrate in space. *J. Fluid Mech.* **454**, 235–261.
- SCHOLLE, M., GASKELL, P.H. & MARNER, F. 2019 A potential field description for gravity-driven film flow over piece-wise planar topography. *Fluids* **4** (2), 82.
- SELLIER, M. 2008 Substrate design or reconstruction from free surface data for thin film flows. *Phys. Fluids* **20** (6), 062106.
- SELLIER, M. & PANDA, S. 2010 Beating capillarity in thin film flows. *Intl J. Numer. Meth. Fluids* **63** (4), 431–448.
- SI, X.A. & XI, J. 2022 Pulmonary oxygen exchange in a rhythmically expanding-contracting alveolus-capillary model. *J. Respir.* **2** (4), 159–173.
- SINGH, G. & TIWARI, N. 2024 Computational study of a thin film flow over a topographical feature using phase-field lattice Boltzmann method. *Phys. Fluids* **36** (3), 032111.
- SLADE, D., VEREMIEIEV, S., LEE, Y.C. & GASKELL, P.H. 2013 Gravity-driven thin film flow: the influence of topography and surface tension gradient on rivulet formation. *Chem. Engng Process.: Process Intensification* **68**, 7–12.
- STILLWAGON, L.E. & LARSON, R.G. 1990 Leveling of thin films over uneven substrates during spin coating. *Phys. Fluids A: Fluid Dyn.* **2** (11), 1937–1944.
- TRIFONOV, Y.Y. 2007 Stability of a viscous liquid film flowing down a periodic surface. *Intl J. Multiphase Flow* **33** (11), 1186–1204.
- TRIFONOV, Y.Y. 2019 Flow of liquid films over a single element of structured packing. Comparison of microtextures of various types. *Thermophys. Aeromech.* **26** (6), 869–878.
- VEREMIEIEV, S., THOMPSON, H.M. & GASKELL, P.H. 2012 Three-dimensional thin film flow over topography: full Navier–Stokes solutions. In *Seventh International Conference on Computational Fluid Dynamics (ICCFD7)*, p. 3304. ICCFD.
- VEREMIEIEV, S., THOMPSON, H.M. & GASKELL, P.H. 2015 Free-surface film flow over topography: full three-dimensional thin element solutions. *Comput. Fluids* **122**, 66–82.
- VEREMIEIEV, S., THOMPSON, H.M., LEE, Y.C. & GASKELL, P.H. 2010 Inertial thin film flow on planar surfaces featuring topography. *Comput. Fluids* **39** (3), 431–450.
- VEREMIEIEV, S., THOMPSON, H.M., LEE, Y.C. & GASKELL, P.H. 2011 Inertial two- and three-dimensional thin film flow over topography. *Chem. Engng Process: Process Intensification* **50** (5–6), 537–542.
- VLACHOGIANNIS, M. & BONTZOZGLOU, V. 2002 Experiments on laminar film flow along a periodic wall. *J. Fluid Mech.* **457**, 133–156.
- WANG, Y.-J., CHEN, S.-C., LIN, Q.-S., ZHANG, X.-M. & CHEN, W.-X. 2020 Numerical simulation and experimental verification of the film-forming behavior of falling film flow down clamped channels with high-viscosity fluid. *Indust. Engng Chem. Res.* **59** (44), 19698–19711.
- WERNZ, J.G. & KRANTZ, G.W. 1976 Studies on the function of the tritosternum in selected Gamasida (Acari). *Can. J. Zool.* **54** (2), 202–213.
- XUE, N. & STONE, H.A. 2021 Draining and spreading along geometries that cause converging flows: viscous gravity currents on a downward-pointing cone and a bowl-shaped hemisphere. *Phys. Rev. Fluids* **6** (4), 043801.